IEEE Access
Multidisciplinary | Rapid Review | Open Access Journal

Received 5 December 2022, accepted 14 January 2023, date of publication 19 January 2023, date of current version 24 January 2023.

Digital Object Identifier 10.1109/ACCESS.2023.3238025

RESEARCH ARTICLE

Maximum-Likelihood-Based Location, Orientation, Transmitted Power, and Antenna Beamwidth Estimator Utilizing the Angle-of-Arrival and Received Power for Spectrum Sharing at Millimeter Wave Bands

PANAWIT HANPINITSAK[1,2,4], (Member, IEEE), KOSUKE MURAKAMI[1], (Student Member, IEEE), JUN-ICHI TAKADA[1], (Senior Member, IEEE), AND KENTARO SAITO[1,3], (Member, IEEE)

[1]Department of Transdisciplinary Science and Engineering, Tokyo Institute of Technology, Tokyo 152-8552, Japan
[2]Department of Computer Engineering, Faculty of Engineering, Khon Kaen University, Khon Kaen 40002, Thailand
[3]Department of Design Engineering and Technology, Tokyo Denki University, Tokyo 120-0026, Japan
[4]Faculty of Business Administration and Accountancy, Khon Kaen University, Khon Kaen 40002, Thailand

Corresponding author: Panawit Hanpinitsak (panaha@kku.ac.th)

This work was supported by the Ministry of Internal Affairs and Communications in Japan under Grant JPJ000254.

ABSTRACT The fifth-generation (5G) system utilizing millimeter wave is available in Japan, but more bandwidth is demanded by the mobile phone operators to accommodate the demand for high data rate. Allocation of the vacant spectrum is impossible due to the past spectrum allocation to other radio systems. For example, 24.25-27.5 GHz has been allocated for the fixed wireless access (FWA) and license exempt small power data communication system in Japan. Although Japanese government is considering to license a part of the band for 5G under the spectrum sharing scheme, the coexistence design is quite challenging due to unavailable operation data of such systems in a form of database for the coexistence study. For this purpose, this paper introduces a maximum-likelihood estimator (MLE), which utilizes the angle-of-arrival (AoA) and received power of the line-of-sight (LOS)/diffraction paths as well as the map database to simultaneously estimate these unknown parameters via the spectrum sensing. It was applied to the measurement data obtained from a sub-urban environment where a commercial fixed wireless access system with similar operational parameters is under operation. Its performance was evaluated for a different number of receiver (Rx) points. The results showed that the parameter estimation accuracy is proportional to the number of receiver points. The distance and orientation errors of 45 m and 5 deg were achieved at 90th percentile with 40 Rx points. Furthermore, the prediction performance of the effective isotropic radiated power (EIRP) was decent, albeit a slight underestimation of the beamwidth.

INDEX TERMS Localization, maximum-likelihood estimator, millimeter wave, angle-of-arrival, spectrum sharing.

I. INTRODUCTION

To accommodate the drastic increase of data traffic and data-hungry wireless applications, the millimeter wave (mmWave) bands with a massive number of antenna elements and large available bandwidth are one of the key components to realize the fifth generation (5G) communication system [1], [2]. Although 24.25-27.5 GHz is allocated for International Mobile Telecommunication (IMT) by Radio Regulations (RR) to serve for 5G globally, these bands have already been utilized by the incumbent fixed wireless systems such as fixed wireless access (FWA) [3], [4] and small

The associate editor coordinating the review of this manuscript and approving it for publication was Chan Hwang See.

power data communication system [5] in Japan. Nevertheless, since the antennas used in these systems have a very high gain and a narrow beamwidth, their coverage is concentrated around the main beam. Thus, it is possible that 5G can share the spectrum with those incumbents by installing 5G base stations sufficiently away from their main beam regions. To quantify this sufficiency, it is inevitable to estimate their coverage area or spatial availability based on their position, orientation, antenna pattern, and transmit power via the radio propagation model [6]. Yet, these pieces of information are sometimes not available or disclosed in the case of temporary or license-exempt systems since they are not recorded in the database. Hence, these parameters need to be estimated before the evaluation of spatial availability.

A few studies have been published that propose a variety of localization techniques for the purpose of spectrum sharing scheme that make use of received signal strength (RSS) or received signal strength indicator (RSSI) [7], [8], [9], [10], [11], [12]. The advantages and disadvantages of these algorithms are summarized in Table 1. Although the majority of these methods were able to achieve good accuracy with low computational complexity, they were only evaluated on simulated data. Thus, it is still an open question how they would perform when using the real measurement data. Furthermore, these studies used the assumption that the system operates in the sub-6 GHz region and that the BS and MS antennas are omni-directional. As a result, they should not be appropriate for localization at mmWave bands because the antenna and channel properties are widely different.

Recently, there have been several investigations of the localization at mmWave bands due to its limited number of significant specular paths, and wideband characteristics which yield more precise angular and delay information than that of lower frequency bands. Table 2 summarizes the methods as well as their advantages and disadvantages in mmWave bands. Some works examined the cooperative localization in the ultra-dense-network and device-to-device scenarios [13]. Still, many of them heavily focused on the massive multiple-input and multiple-output (MIMO) localization and orientation estimation, where the path parameters such as the angle-of-arrival (AoA), angle-of-departure (AoD), and time-of-arrival (ToA) could be accurately estimated [14]. These path parameters and sometimes the received signal strength indicator (RSSI) and environment map were extracted and exploited for positioning in [15], [16], [17], [18], [19], [20], [21], [22], [23], [24], [25], [26], [27], [28], and [29]. In contrast, the direct localization using the channel properties was proposed in [30] and [31]. In other works, [32] and [33] estimated the vehicle location, orientation, and environment using AoA, AoD, ToA, and belief propagation method. In [34], [35], and [36], the location of the mobile user, as well as the environment map, were simultaneously estimated via the angle-difference-of-arrival, imaging technique, and map-based channel model, respectively. The re-configurable intelligent surface (RIS) was used to enhance the localization accuracy in [37] and [38]. Reference [39] considered beamforming (BF) to improve the positioning accuracy. Furthermore, machine learning techniques such as neural networks were used for the localization in [40], [41], and [42].

Although these past works provide effective localization methods for different scenarios via a wide range of techniques, they are difficult to be applied for the localization of incumbent fixed systems for spectrum sharing due to four main reasons. First, these terminals could be installed anywhere and their location could be changed periodically. Therefore, the fingerprinting or machine-learning-based methods might not be usable as it is computationally infeasible to conduct the training phase for all possible terminal positions. Second, most algorithms assume that the ToA, AoD, and channel matrix could be used for the localization by exploiting the wideband and massive MIMO characteristics of the transceivers. However, in the incumbent system, the bandwidth is normally in the order of tens of MHz and it is a single antenna [3], [4]. Thus, these variables could not be utilized. Third, since some of these methods are derived specifically for 5G scenarios, it may only be suitable in the case where the base station is usually a few meters above the ground and the coverage area is small. In contrast, the fixed systems are usually installed at several meters above the ground which causes the major propagation mechanisms to be different. Thus, it is still an open question whether these approaches could be successfully applied to the fixed system case. Finally, although many of the massive MIMO papers consider the position as well as the array orientation estimation, these methods do not estimate both the antenna pattern and the transmit power, which are unknown and thus required for the availability estimation in the space domain. To the best knowledge of the authors, the method that could simultaneously estimate the location, orientation, transmit power, and antenna pattern of the existing system for the coexistence at mmWave bands have not been considered in the open literature.

In light of these aforementioned issues of the previous works' applicability for fixed system localization, this paper introduces the maximum-likelihood estimator (MLE), where the location, antenna pattern, direction, and transmit power are simultaneously estimated based on maximizing the joint Gaussian probability density function of the azimuth of arrival (AzoA), the elevation of arrival (EloA), and received power of the paths. Since the over-roof top diffraction is one of the major mechanisms when the transmitter (Tx) is mounted at high elevation [43], [44], [45], [46], which is normally the case of fixed systems, the diffraction paths are considered as well as the line-of-sight (LOS) for the localization. Similar to the conventional AoA-based MLE [47], [48], the AzoA and EloA are calculated based on the geometry between Tx and receiver (Rx) positions, whereas the received power is computed by using free space equation [49] and uniform theory of diffraction (UTD) [50] for LOS and

TABLE 1. Advantages and disadvantages of localization methods in spectrum sharing scheme.

Paper	Method	Advantages	Limits
[7], [8]	Machine learning-based localization using RSS	Could estimate the location and transmit power of multiple transmitters simultaneously with acceptable computation time	- Suitable for the localization in the sub-6 GHz band with omni-directional antennas - Do not estimate the antenna orientation like that of mmWave bands - Evaluated using only simulated data
[9]	RSS smoothing		
[10]	Trilateration with annular region	Able to localize accurately while only utilizing three mobile nodes	
[11]	Maximum-likelihood estimator using RSS	Can estimate the coverage area by constructing the radio environment map via interpolation methods	
[12]	Dynamic signal strength mapping		

TABLE 2. Advantages and disadvantages of localization methods in mmWave bands.

Paper	Method	Advantages	Limits
[13]	Cooperative device to device MIMO localization using one or more signal metrics	Can increase localization accuracy and reduce the time delay	May need to rely on other mobile terminals for accurate localization
[15]–[25]	MIMO/massive MIMO localization/orientation estimation via the use of AoA, AoD, ToA, and/or RSSI	Can achieve good accuracy by exploiting good delay and/or angular resolutions from both LOS/NLOS paths and using only a single base station or access point	Assume that array geometry, ToA, AoD, and/or channel gain are known
[26], [27]	Environment map assisted localization using multipath parameters	Able to achieve high accuracy even in NLOS scenarios by utilizing the map to assist with localization	Assume that LOS/reflection are the major propagation mechanisms and only simulated data are used for evaluation
[28]	Combined LOS/NLOS based localization using RSS, ToA, AoA	Can achieve good accuracy by utilizing both LOS and NLOS paths in the localization	
[29]	Explore LOS scenario localization performance using simple weighted least square methods	Low computational complexity	Do not consider NLOS scenario and only simulated data are used for evaluation
[30]	Direct massive MIMO localization exploiting channel properties such as AoA and waveform curvature	Can discriminate between LOS and NLOS paths and achieve good accuracy even in narrowband settings	High computational complexity and assume that the channel transfer function can be obtained
[31]		Can carry out one-shot localization by exploiting the waveform curvature	Assume that the channel transfer function is known and near-field condition is met
[32], [33]	Vehicle localization and orientation estimation using belief propagation filter and factor graph methods	Able to estimate position, orientation, environment map, as well as clock bias by using only a single base station	Designed specifically for vehicular tracking and require AoD information for localization
[34]	Estimate the location and environment map using angle-difference-of-arrival	Low computational complexity with no special signal processing required	Designed specifically for indoor localization with APs that support beam training and beam tracking
[35]	Estimate the location and environment map using mmWave imaging technique	Can rely on a single antenna array to locate NLOS users where their signals have multiple reflections	Assume that LOS/reflection are the major propagation mechanisms and large bandwidth is necessary for accurate ToA estimation
[36]	Estimate the location and environment map using map-based channel model	Can create environment mapping and detect obstacles based only on the channel measurements	
[37], [38]	Localization with the aid of re-configurable intelligent surface (RIS)	Can achieve much higher accuracy than the case without RIS	Require assistance from the RIS and assume that only single bounce reflection occurs from the RIS
[39]	Successive localization and active beamforming using MIMO system	Can jointly estimate the instantaneous channel state and the UE location, as well as optimizing BF weights	Require MIMO antennas with active BF capabilities and assume that the frame structure of the system is known
[40]–[42]	Fingerprint and/or machine learning methods such as deep neural network	Capable of learning complex functions that could improve localization accuracy	May need to conduct training phase for several terminal positions to ensure sufficient accuracy
This work	MLE-based location, orientation, Tx power, and beamwidth estimator	Capable of estimating antenna beamwidth and transmit power without requiring the ToA and AoD information	Designed specifically for spectrum sharing scenario where the fixed systems are mounted at several meters above the ground

diffraction paths, respectively. It is considered to be the substantial extension of the authors' work in [51]. However, in [51], only the LOS between Tx-Rx was assumed, which is not realistic in the sub-urban or urban environment. Furthermore, the antenna pattern estimation was not taken into the account. The other contributions and enhancements are divided into three points: First, from the angular power spectrum of each Rx, two peaks with opposite direction

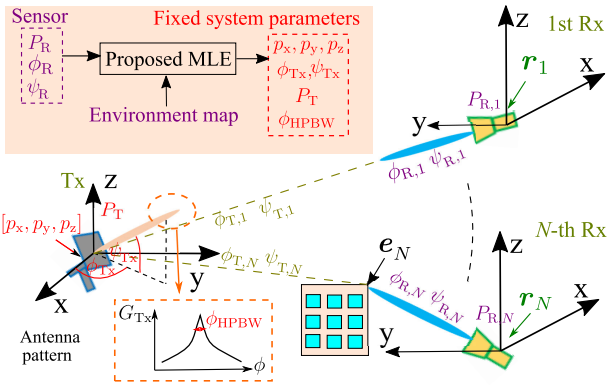

FIGURE 1. Localization Model and Concept.

are estimated and their propagation mechanisms are distinguished using the KPowerMeans [52] clustering algorithm. Second, not only the LOS power are computed, but also the diffraction edge detection and calculation via UTD are performed with the assistance of the map database. Finally, the Jacobian matrix is derived, and the iterative Levenberg-Marquardt (LM) [53] method is applied to optimize the joint AzoA-EloA-received power likelihood function in a computationally efficient manner. The proposed method was evaluated and compared with the conventional MLE [47], [48] using the outdoor sub-urban environment measurement. The results implied that the performances normally increased as the number of Rx points increased. Moreover, the proposed MLE mostly improved the accuracy of the conventional MLE in the vertical direction if there were steep diffraction paths at some Rx points.

The rest of the paper is organized as follows. The proposed localization model and algorithm are described in details in Section II. The specifications of transmitter and receivers as well as the measurement campaign and RT parameters description are provided in Section III. In Section IV, the validation of the proposed method and comparison with the conventional MLE method were carried out. Finally, Section V summarizes the key findings of this paper.

II. PROPOSED LOCALIZATION METHOD

A. MAXIMUM-LIKELIHOOD BASED LOCALIZATION AND SIGNAL MODEL

Fig. 1 illustrates the localization model and concept where the Tx or emitter is located at $\boldsymbol{p} = \left[p_{\mathrm{x}}, p_{\mathrm{y}}, p_{\mathrm{z}}\right]^T$. Assuming that it is mounted with the pencil-beam directional antenna where its half-power beamwidth (HPBW) in the azimuth and elevation plane are the same, the normalized antenna gain envelope pattern in the dB scale adopted from the ITU-R F.1336 model is expressed by [54]

$$G_{\mathrm{Tx}}(\phi_{\mathrm{HPBW}}, \phi, \psi) = \begin{cases} -12x^2 & , x < 1.152 \\ -15 - 15\log_{10} x & , 1.152 \leq x, \end{cases} \quad (1)$$

where

$$x = \frac{\cos^{-1}(\cos\phi\cos\psi)}{\phi_{\mathrm{HPBW}}}, \quad (2)$$

and ϕ_{HPBW}, ϕ, and ψ are the HPBW, azimuth and elevation angles, respectively. Its transmitted power is P_{T} and the direction of main beam is pointed at the azimuth and elevation angles ϕ_{Tx} and ψ_{Tx}, respectively. The receiver is placed at N different positions. The k-th receiver position is depicted as $\boldsymbol{r}_k = \left[r_{\mathrm{x},k}, r_{\mathrm{y},k}, r_{\mathrm{z},k}\right]^T$. Two types of receivers are assumed: One utilizes the fan-beam antenna mounted on the one-dimensional rotator [55]; the other exploits pencil-beam antenna mounted on the two-dimensional rotator. These will be called the first Rx system and second Rx system, respectively. Two types of receivers are used for different purposes: First Rx system is mainly used for the mobile sensor for initial detection of Tx, while second Rx system is mainly used for the fixed sensor for detail search of Tx direction. The elevation gain pattern of the first system is $G_{\mathrm{Rx},1}(\psi)$. The maximum gain of the second system is $G_{\mathrm{Rx},2,\max}$. The number of positions for the respective receivers are N_1 and N_2. System 1 records only the azimuth angle $\tilde{\phi}_{\mathrm{R},k}$, whereas system 2 records both azimuth $\tilde{\phi}_{\mathrm{R},k}$ and elevation angle $\tilde{\psi}_{\mathrm{R},k}$. $\tilde{P}_{\mathrm{R},k}$ denotes the peak received power. Two types of paths are assumed: LOS and over-roof top diffraction. Define

$$\begin{aligned} \boldsymbol{q} &= \left[\boldsymbol{p}^T, \phi_{\mathrm{Tx}}, \psi_{\mathrm{Tx}}, P_{\mathrm{T}}, \phi_{\mathrm{HPBW}}\right]^T \\ &= \left[p_{\mathrm{x}}, p_{\mathrm{y}}, p_{\mathrm{z}}, \phi_{\mathrm{Tx}}, \psi_{\mathrm{Tx}}, P_{\mathrm{T}}, \phi_{\mathrm{HPBW}}\right]^T \end{aligned} \quad (3)$$

as the vector of unknown Tx parameters to be estimated, the signal models of the received angles at the k-th position can be expressed by

$$\tilde{\phi}_{\mathrm{R},k} = \phi_{\mathrm{R},k}(\boldsymbol{q}) + w_{\phi} \quad (4)$$

$$\tilde{\psi}_{\mathrm{R},k} = \psi_{\mathrm{R},k}(\boldsymbol{q}) + w_{\psi}, \quad (5)$$

where w_{ϕ} and w_{ψ} are the Gaussian distributed error with zero mean and variance σ_{ϕ}^2 and σ_{ψ}^2. $\phi_{\mathrm{R},k}(\boldsymbol{q})$ and $\psi_{\mathrm{R},k}(\boldsymbol{q})$ represent the calculated azimuth and elevation angle. In case of LOS path, they are calculated from the geometry of $\boldsymbol{p}$ and $\boldsymbol{r}_k$ by [48]

$$\phi_{\mathrm{R},k}(\boldsymbol{q}) = \tan^{-1}\left(\frac{p_{\mathrm{y}} - r_{\mathrm{y},k}}{p_{\mathrm{x}} - r_{\mathrm{x},k}}\right) \quad (6)$$

$$\psi_{\mathrm{R},k}(\boldsymbol{q}) = \sin^{-1}\left(\frac{p_{\mathrm{z}} - r_{\mathrm{z},k}}{\|\boldsymbol{r}_k - \boldsymbol{p}\|}\right) \quad (7)$$

In case of diffraction path, $\phi_{\mathrm{R},k}(\boldsymbol{q})$ calculation follows (6). However, $\psi_{\mathrm{R},k}(\boldsymbol{q})$ has to be geometrically obtained from $\boldsymbol{r}_k$ and estimated edge location $\boldsymbol{e}_k(\boldsymbol{q}) = \left[e_{\mathrm{x},k}(\boldsymbol{q}), e_{\mathrm{y},k}(\boldsymbol{q}), e_{\mathrm{z},k}(\boldsymbol{q})\right]^T$ by

$$\psi_{\mathrm{R},k}(\boldsymbol{q}) = \sin^{-1}\left(\frac{e_{\mathrm{z},k}(\boldsymbol{q}) - r_{\mathrm{z},k}}{\|\boldsymbol{r}_k - \boldsymbol{e}_k(\boldsymbol{q})\|}\right) \quad (8)$$

Similarly, the signal model of the received power in dB at the k-th position can be written by

$$\tilde{P}_{\mathrm{R},k} = P_{\mathrm{R},k}(\boldsymbol{q}) + w_{\mathrm{P}} \quad (9)$$

where $P_{\mathrm{R},k}(\boldsymbol{q})$ is the calculated received power in dB to be defined below. w_{P} is the Gaussian error with zero mean and variance σ_{P}^2. The received power $P_{\mathrm{R},k}$ in case of the first system in dB is calculated by

$$P^{\mathrm{f}}_{\mathrm{R},k}(\boldsymbol{q}) = P_{\mathrm{T}} + G_{\mathrm{Tx}}(\phi_{\mathrm{HPBW}}, \phi_{\mathrm{T},k}(\boldsymbol{q}) - \phi_{\mathrm{Tx}}, \psi_{\mathrm{T},k}(\boldsymbol{q}) - \psi_{\mathrm{Tx}}) - L_{\mathrm{p},k}(\boldsymbol{q}) + G_{\mathrm{Rx},1}(\psi_{\mathrm{R},k}(\boldsymbol{q})), \tag{10}$$

Similarly, for the second system, the received power in dB is computed as

$$P^{\mathrm{s}}_{\mathrm{R},k}(\boldsymbol{q}) = P_{\mathrm{T}} + G_{\mathrm{Tx}}(\phi_{\mathrm{HPBW}}, \phi_{\mathrm{T},k}(\boldsymbol{q}) - \phi_{\mathrm{Tx}}, \psi_{\mathrm{T},k}(\boldsymbol{q}) - \psi_{\mathrm{Tx}}) - L_{\mathrm{p},k}(\boldsymbol{q}) + G_{\mathrm{Rx},2,\max}, \tag{11}$$

where $\phi_{\mathrm{T},k}(\boldsymbol{q})$ and $\psi_{\mathrm{T},k}(\boldsymbol{q})$ are the azimuth of departure and elevation of departure based on the Cartesian coordinate system depicted in Fig. 1. In case of LOS, it is simply computed by

$$\phi_{\mathrm{T},k}(\boldsymbol{q}) = \phi_{\mathrm{R},k}(\boldsymbol{q}) \tag{12}$$

$$\psi_{\mathrm{T},k}(\boldsymbol{q}) = -\psi_{\mathrm{R},k}(\boldsymbol{q}). \tag{13}$$

Note that since the xy coordinates of the Tx and Rx differ by 180 degrees as shown in Fig. 1, the AzoA and azimuth of departure of LOS paths are the same. In case of diffraction paths, they are calculated from $\boldsymbol{p}$ and $\boldsymbol{e}_k(\boldsymbol{q})$ by

$$\phi_{\mathrm{T},k}(\boldsymbol{q}) = \tan^{-1}\left(\frac{p_{\mathrm{y}} - e_{\mathrm{y},k}(\boldsymbol{q})}{p_{\mathrm{x}} - e_{\mathrm{x},k}(\boldsymbol{q})}\right) \tag{14}$$

$$\psi_{\mathrm{T},k}(\boldsymbol{q}) = \sin^{-1}\left(\frac{e_{\mathrm{z},k}(\boldsymbol{q}) - p_{\mathrm{z}}}{\|\boldsymbol{e}_k - \boldsymbol{p}\|}\right). \tag{15}$$

From (10) and (11), $L_{\mathrm{p},k}(\boldsymbol{q})$ is the loss due to propagation. In case of LOS, it is computed based on free space path loss in dB [49] by

$$L_{\mathrm{p},k}(\boldsymbol{q}) = 10\log_{10}\left(\frac{4\pi\,\|\boldsymbol{p} - \boldsymbol{r}_k\|}{\lambda}\right)^2, \tag{16}$$

where λ is the signal wavelength. In case of diffraction, it is obtained from UTD [50] in dB by

$$L_{\mathrm{p},k}(\boldsymbol{q}) = 10\log_{10}\left(\left(\frac{4\pi s'_k(\boldsymbol{q})}{\lambda}\right)^2 \frac{s_k(\boldsymbol{q})(s'_k(\boldsymbol{q}) + s_k(\boldsymbol{q}))}{s'_k(\boldsymbol{q})D_k^2(\boldsymbol{q})}\right) \tag{17}$$

where $s_k(\boldsymbol{q}) = \|\boldsymbol{e}_k(\boldsymbol{q}) - \boldsymbol{r}_k\|$ and $s'_k(\boldsymbol{q}) = \|\boldsymbol{p} - \boldsymbol{e}_k(\boldsymbol{q})\|$ are the distance from edge to Rx and Tx, respectively. $D_k(\boldsymbol{q})$ is expressed by

$$D_k(\boldsymbol{q}) = \frac{\left|F\left(\frac{4\pi}{\lambda}\frac{s'_k(\boldsymbol{q})s_k(\boldsymbol{q})}{s'_k(\boldsymbol{q})+s_k(\boldsymbol{q})}\sin^2\left(\frac{\alpha_k(\boldsymbol{q})}{2}\right)\right)\right|}{\frac{4\pi}{\sqrt{\lambda}}\sin\left(\frac{\alpha_k(\boldsymbol{q})}{2}\right)} \tag{18}$$

where

$$\alpha_k(\boldsymbol{q}) = \pi - (\beta_k(\boldsymbol{q}) - \beta'_k(\boldsymbol{q})) \tag{19}$$

$F(.)$ is the Fresnel integral. $\beta_k(\boldsymbol{q})$ and $\beta'_k(\boldsymbol{q})$ are the angle between edge and Rx and Tx which is calculated by

$$\beta_k(\boldsymbol{q}) = 2\pi - \cos^{-1}\left(\frac{p_{\mathrm{z}} - e_{\mathrm{z},k}(\boldsymbol{q})}{\|\boldsymbol{e}_k(\boldsymbol{q}) - \boldsymbol{r}_k\|}\right) \tag{20}$$

$$\beta'_k(\boldsymbol{q}) = \cos^{-1}\left(\frac{e_{\mathrm{z},k}(\boldsymbol{q}) - p_{\mathrm{z}}}{\|\boldsymbol{e}_k(\boldsymbol{q}) - \boldsymbol{p}\|}\right) \tag{21}$$

From (4), (5), and (9), the vectorized model that include all Rx points could be expressed by

$$\tilde{\boldsymbol{\phi}}_{\mathrm{R}} = \boldsymbol{\phi}_{\mathrm{R}}(\boldsymbol{q}) + \boldsymbol{w}_{\phi} \tag{22}$$

$$\tilde{\boldsymbol{\psi}}_{\mathrm{R}} = \boldsymbol{\psi}_{\mathrm{R}}(\boldsymbol{q}) + \boldsymbol{w}_{\psi} \tag{23}$$

$$\tilde{\boldsymbol{P}}_{\mathrm{R}} = \boldsymbol{P}_{\mathrm{R}}(\boldsymbol{q}) + \boldsymbol{w}_{\mathrm{P}} \tag{24}$$

where $\tilde{\boldsymbol{\phi}}_{\mathrm{R}} = \left[\tilde{\phi}_{\mathrm{R},1}, \ldots, \tilde{\phi}_{\mathrm{R},N}\right]^T$, $\tilde{\boldsymbol{\psi}}_{\mathrm{R}} = \left[\tilde{\psi}_{\mathrm{R},1}, \ldots, \tilde{\psi}_{\mathrm{R},N_2}\right]^T$, and $\tilde{\boldsymbol{P}}_{\mathrm{R}} = \left[\tilde{P}_{\mathrm{R},1}, \ldots, \tilde{P}_{\mathrm{R},N}\right]^T$ are the vectors of measured azimuth angle, elevation angle, and received power. $\boldsymbol{\phi}_{\mathrm{R}}(\boldsymbol{q}) = \left[\phi_{\mathrm{R},1}(\boldsymbol{q}), \ldots, \phi_{\mathrm{R},N}(\boldsymbol{q})\right]^T$, $\boldsymbol{\psi}_{\mathrm{R}}(\boldsymbol{q}) = \left[\psi_{\mathrm{R},1}(\boldsymbol{q}), \ldots, \psi_{\mathrm{R},N_2}(\boldsymbol{q})\right]^T$, and $\boldsymbol{P}_{\mathrm{R}}(\boldsymbol{q}) = \left[P_{\mathrm{R},1}(\boldsymbol{q}), \ldots, P_{\mathrm{R},N}(\boldsymbol{q})\right]^T$ are the vectors of calculated azimuth angle in radian, elevation angle in radian, and received power in dB. $\boldsymbol{w}_{\phi}$, $\boldsymbol{w}_{\psi}$, and $\boldsymbol{w}_{\mathrm{P}}$ are the vectors of Gaussian errors.

The total signal model could then be constructed by

$$\tilde{\boldsymbol{z}} = \boldsymbol{z}(\boldsymbol{q}) + \boldsymbol{w}, \tag{25}$$

where

$$\tilde{\boldsymbol{z}} = \left[\tilde{\boldsymbol{\phi}}_{\mathrm{R}}, \tilde{\boldsymbol{\psi}}_{\mathrm{R}}, \tilde{\boldsymbol{P}}_{\mathrm{R}}\right]^T, \tag{26}$$

$$\boldsymbol{z}(\boldsymbol{q}) = \left[\boldsymbol{\phi}_{\mathrm{R}}(\boldsymbol{q}), \boldsymbol{\psi}_{\mathrm{R}}(\boldsymbol{q}), \boldsymbol{P}_{\mathrm{R}}(\boldsymbol{q})\right]^T, \tag{27}$$

$$\boldsymbol{w} = \left[\boldsymbol{w}_{\phi}, \boldsymbol{w}_{\psi}, \boldsymbol{w}_{\mathrm{P}}\right]^T. \tag{28}$$

The location of the Tx could be obtained by maximizing the likelihood function as follows

$$\hat{\boldsymbol{q}} = \arg\max_{\boldsymbol{q}} p(\tilde{\boldsymbol{z}}; \boldsymbol{q}), \tag{29}$$

where

$$p(\tilde{\boldsymbol{z}}; \boldsymbol{q}) = \frac{1}{\sqrt{(2\pi)^M |\boldsymbol{K}|}} \exp\left(-\frac{1}{2}[\tilde{\boldsymbol{z}} - \boldsymbol{z}(\boldsymbol{q})]^T \boldsymbol{K}^{-1}[\tilde{\boldsymbol{z}} - \boldsymbol{z}(\boldsymbol{q})]\right) \tag{30}$$

where $\boldsymbol{K} = \mathrm{diag}\left(\sigma_{\phi}^2, .., \sigma_{\phi}^2, \sigma_{\psi}^2, \ldots, \sigma_{\psi}^2, \sigma_{\mathrm{P}}^2, \ldots, \sigma_{\mathrm{P}}^2\right)$. Since the term in front of exponential is constant, the estimator could be simplified by

$$A_{\mathrm{ML,proposed}}(\boldsymbol{q}) = [\tilde{\boldsymbol{z}} - \boldsymbol{z}(\boldsymbol{q})]^T \boldsymbol{K}^{-1}[\tilde{\boldsymbol{z}} - \boldsymbol{z}(\boldsymbol{q})] \tag{31}$$

$$\hat{\boldsymbol{q}} = \arg\min_{\boldsymbol{q}} \left(A_{\mathrm{ML,proposed}}(\boldsymbol{q})\right). \tag{32}$$

In the subsequent sections, the procedure to obtain $\hat{\boldsymbol{q}}$ from the angular power spectrum data will be explained in details.

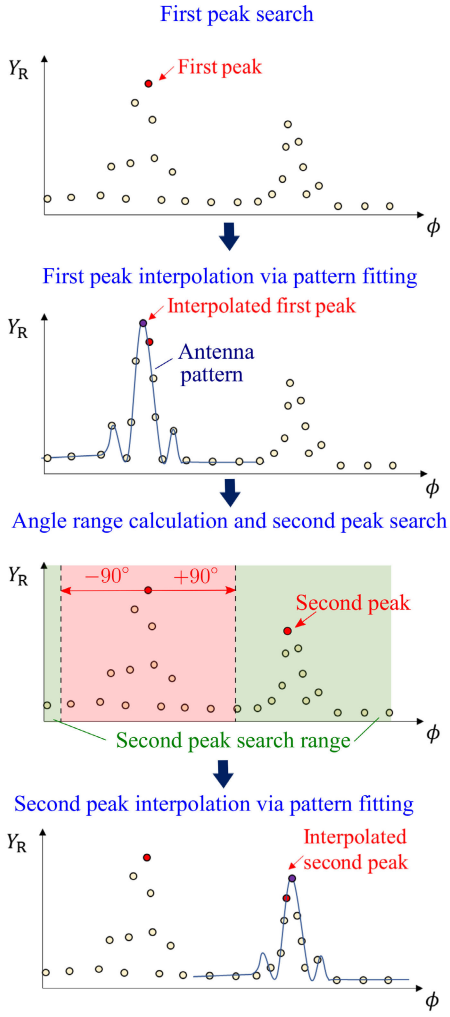

FIGURE 2. Illustration of two peak search.

B. PATH DETECTION AND PROPAGATION MECHANISM IDENTIFICATION

Due to the narrow beamwidth of the Tx antenna which is mounted several meters above the ground, it is thought that there would be two major mechanisms observed at the Rx: 1. LOS or diffraction, 2. Backscattering from the opposite building. Thus, in the first step, two peaks with opposite direction are identified. Fig. 2 illustrates the two peak search method. Assuming that the angular power spectrum of the first system and second system at the k-th position are $Y_{\mathrm{R},1,k}(\phi)$ and $Y_{\mathrm{R},2,k}(\phi, \psi)$, where ϕ and ψ are the azimuth and elevation angle of the antenna, the first peak is found by

$$\begin{cases} \tilde{\phi}_{\mathrm{R},1,k} = \arg\max\limits_{\phi} \left(Y_{\mathrm{R},1,k}(\phi)\right) & \text{System 1} \\ [\tilde{\phi}_{\mathrm{R},1,k}, \tilde{\psi}_{\mathrm{R},1,k}] = \arg\max\limits_{\phi,\psi} \left(Y_{\mathrm{R},2,k}(\phi, \psi)\right) & \text{System 2} \end{cases} \tag{33}$$

Then, the first peak power is found by

$$\begin{cases} \tilde{P}_{\mathrm{R},1,k} = Y_{\mathrm{R},1,k}(\tilde{\phi}_{\mathrm{R},1,k}) & \text{System 1} \\ \tilde{P}_{\mathrm{R},1,k} = Y_{\mathrm{R},2,k}(\tilde{\phi}_{\mathrm{R},1,k}, \tilde{\psi}_{\mathrm{R},1,k}) & \text{System 2} \end{cases} \tag{34}$$

To find the second peak with opposite direction, the azimuth angle is limited by extending the angle range from $\tilde{\phi}_{\mathrm{R},1,k} - 90°$ to $\tilde{\phi}_{\mathrm{R},1,k} + 90°$ as shown in Fig. 2. Then, the second peak is searched outside this range, which is expressed by

$$\begin{cases} \tilde{\phi}_{\mathrm{R},2,k} = \arg\max\limits_{\phi \in B} \left(Y_{\mathrm{R},1,k}(\phi)\right) & \text{System 1} \\ [\tilde{\phi}_{\mathrm{R},2,k}, \tilde{\psi}_{\mathrm{R},2,k}] = \arg\max\limits_{\phi \in B, \psi} \left(Y_{\mathrm{R},2,k}(\phi, \psi)\right) & \text{System 2} \end{cases} \tag{35}$$

where B is the set of angles outside the range $[\tilde{\phi}_{\mathrm{R},1,k} - 90°, \tilde{\phi}_{\mathrm{R},1,k} + 90°]$.

Similar to the first peak, the second peak power is then computed by

$$\begin{cases} \tilde{P}_{\mathrm{R},2,k} = Y_{\mathrm{R},1,k}(\tilde{\phi}_{\mathrm{R},2,k}) & \text{System 1} \\ \tilde{P}_{\mathrm{R},2,k} = Y_{\mathrm{R},2,k}(\tilde{\phi}_{\mathrm{R},2,k}, \tilde{\psi}_{\mathrm{R},2,k}) & \text{System 2} \end{cases} \tag{36}$$

Inspired by [56] and [57], a more precise angle and peak power could be found by interpolating the measured data with the normalized antenna gain pattern as shown in Fig. 2. This is done by fitting the few angular bins around the peak in the least square way [57]. To be exact, three points are considered for system 1: $\phi_{\mathrm{R,max}} - \Delta\phi$, $\phi_{\mathrm{R,max}}$, and $\phi_{\mathrm{R,max}} + \Delta\phi$, where $\phi_{\mathrm{R,max}}$ and $\Delta\phi$ are the peak value and angular steps in azimuth domain. For system 2, in azimuth-elevation angle pairs, five points are considered: $(\phi_{\mathrm{R,max}} - \Delta\phi, \psi_{\mathrm{R,max}})$, $(\phi_{\mathrm{R,max}}, \psi_{\mathrm{R,max}})$, $(\phi_{\mathrm{R,max}} + \Delta\phi, \psi_{\mathrm{R,max}})$, $(\phi_{\mathrm{R,max}}, \psi_{\mathrm{R,max}} - \Delta\psi)$, and $(\phi_{\mathrm{R,max}}, \psi_{\mathrm{R,max}} + \Delta\psi)$, where $\psi_{\mathrm{R,max}}$ and $\Delta\psi$ are the peak value and angular steps in elevation domain.

In the next step, the LOS/diffraction peaks are distinguished from backscattering peaks using clustering. Fig. 3 shows the concept. If two opposite peaks from several Rx points are clustered, two distinct groups should be observed as the AoA of the peaks with the same mechanism should be similar. To identify the group and separate them from each other, clustering is needed. Similar to the authors' work in [58], the KPowerMeans clustering algorithm [52] with deterministic initialization method [59] is adapted and utilized. Firstly, the two peaks of all Rx points are stacked into matrix $\boldsymbol{X}$ by

$$\boldsymbol{X} = \begin{bmatrix} \cos\tilde{\phi}_{\mathrm{R},1,1} & \sin\tilde{\phi}_{\mathrm{R},1,1} \\ \vdots & \vdots \\ \cos\tilde{\phi}_{\mathrm{R},1,N} & \sin\tilde{\phi}_{\mathrm{R},1,N} \\ \cos\tilde{\phi}_{\mathrm{R},2,1} & \sin\tilde{\phi}_{\mathrm{R},2,1} \\ \vdots & \vdots \\ \cos\tilde{\phi}_{\mathrm{R},2,N} & \sin\tilde{\phi}_{\mathrm{R},2,N} \end{bmatrix} \tag{37}$$

Note that the directional cosine is used to avoid the angular periodicity issues [60]. Let $\boldsymbol{x}_k$ be the k-th row of matrix $\boldsymbol{X}$, which denotes the parameter vector, and P_k be the corresponding peak power, KPowerMeans algorithm is based on minimizing the total power-weighted intra-cluster

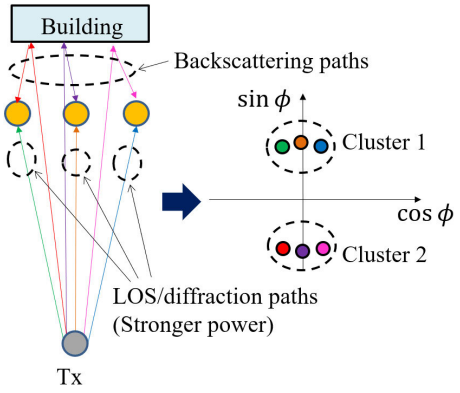

FIGURE 3. Discrimination of propagation mechanisms using clustering.

distance D by

$$D = \min \sum_{k} P_k \cdot \|\boldsymbol{x}_k - \boldsymbol{c}_k\|, \tag{38}$$

where $\boldsymbol{c}_k$ is the cluster centroid of k-th data which is the power-weighted mean of the parameter vector that belongs to that cluster. It should be noted that the Euclidean distance is used instead of the multipath component distance used in [52]. Furthermore, the number of clusters is fixed to two which corresponds to LOS/diffraction and backscattering. Thus, the quality evaluation of the clustering results at different cluster number by cluster validation indices is not required. The rest of the algorithm implementation is the same as [52]. After the clusters are obtained, the LOS/diffraction cluster could be identified simply by choosing the cluster with a higher total power.

C. COARSE SEARCH AND DIFFRACTION EDGE DETECTION

After the LOS/diffraction cluster is obtained, it is utilized for the initialization, coarse search and diffraction edge detection. However, this cluster may contain outliers that correspond to the scattering in the horizontal plane. These outliers may cause errors since the received power calculation does not consider the horizontal scattering. Therefore, they should first be removed from the analysis by two steps. Firstly, assuming that the KPowerMeans clustering algorithm yields a LOS/diffraction cluster that correspond to N_{L} receiver positions $\boldsymbol{r}_1, \boldsymbol{r}_2, \ldots, \boldsymbol{r}_{N_{\mathrm{L}}}$ with the azimuth angle $\tilde{\phi}_{\mathrm{R},1}, \tilde{\phi}_{\mathrm{R},2}, \ldots, \tilde{\phi}_{\mathrm{R},N_{\mathrm{L}}}$ and received power in dB scale $\tilde{P}_{\mathrm{R},1}, \tilde{P}_{\mathrm{R},2}, \ldots, \tilde{P}_{\mathrm{R},N_{\mathrm{L}}}$, the initial Tx main beam azimuth direction is estimated by

$$\hat{\phi}_{\mathrm{T,initial}} = \frac{\sum_{k=1}^{N_{\mathrm{L}}} 10^{\tilde{P}_{\mathrm{R},k}} \cdot \tilde{\phi}_{\mathrm{R},k}}{\sum_{k=1}^{N_{\mathrm{L}}} 10^{\tilde{P}_{\mathrm{R},k}}}. \tag{39}$$

Secondly, the points where the azimuth angle is between $\hat{\phi}_{\mathrm{T,initial}} - \delta_{\Phi}$ and $\hat{\phi}_{\mathrm{T,initial}} + \delta_{\Phi}$ are included in the next step, where δ_{Φ} is the angle threshold.

For simplicity, the initial main beam direction in elevation is set to zero.

$$\hat{\psi}_{\mathrm{T,initial}} = 0. \tag{40}$$

Next, the initial Tx position is attained by using conventional MLE [47], [48] by

$$\hat{\boldsymbol{p}}_{\mathrm{initial,MLE}} = \arg\min_{\boldsymbol{p}} (A_{\mathrm{ML}}(\boldsymbol{p})), \tag{41}$$

where $A_{\mathrm{ML}}(\boldsymbol{p})$ is the conventional ML cost function [47], [48], which is expressed by (57) in Appendix B. It should also be noted that the iterative LM method [53] is used to optimize this cost function in which pseudo-linear estimator (PLE) [47], [48] (see Appendix A) is used as the initial value.

Subsequently, the coarse search with diffraction building edge detection is performed to initialize the Tx parameters in $\boldsymbol{q}$ for the fine search. The edge detection requires the map database which will be explained in the next Section. The flow chart of the coarse search and edge detection is shown in Fig. 4. In the first step, the coarse search grid of p_{z}, P_{T}, and ϕ_{HPBW} are created. Note that the coarse grids of horizontal positions (p_{x} and p_{y}) are not created, rather they are obtained from conventional MLE using (41) to save simulation time. This is because it is found out that conventional MLE had sufficient horizontal positions localization accuracy. Secondly, a set of Tx parameters in $\boldsymbol{q}$ is created from (39)-(41) and the values in the coarse search grids of three parameters explained above. At each Rx point, all the buildings that intersect with the straight line from Tx to Rx are identified as shown by the orange buildings in Fig. 5. If there is no building that intersects with this straight line, only the LOS power is calculated using free space (16). Otherwise, assuming that at the k-th Rx, there is $L_k(\boldsymbol{q})$ number of intersected building edges, and the l-th edge is at the position $\boldsymbol{e}_l(\boldsymbol{q}) = [e_{\mathrm{x},l}(\boldsymbol{q}), e_{\mathrm{y},l}(\boldsymbol{q}), e_{\mathrm{z},l}(\boldsymbol{q})]^T$, one edge which has the maximum height is chosen as illustrated by the orange building with purple edge in Fig. 5.

$$\hat{l}_k(\boldsymbol{q}) = \mathrm{argmax}_{l \in \{1,2,\ldots,L_k(\boldsymbol{q})\}} e_{\mathrm{z},l}(\boldsymbol{q}) \tag{42}$$

$$\hat{\boldsymbol{e}}_k(\boldsymbol{q}) = \boldsymbol{e}_{\hat{l}_k(\boldsymbol{q})}(\boldsymbol{q}) \tag{43}$$

The edge with the maximum height is chosen because the diffraction loss should be dominated by that edge. Then, the diffraction power (17) and elevation angle (8) is computed from the estimated edge as well as the LOS power (16) and elevation angle (7). Finally, either the diffraction or LOS path is chosen based on the one that minimizes the power error (system 1) or joint power and elevation angle error (system 2), which is expressed by

$$\varepsilon_k(\boldsymbol{q}) = \begin{cases} \dfrac{\left(\tilde{P}_{\mathrm{R},k} - P_{\mathrm{R},k}(\boldsymbol{q})\right)^2}{\sigma_{\mathrm{P}}^2} & \text{System 1} \\ \dfrac{\left(\tilde{P}_{\mathrm{R},k} - P_{\mathrm{R},k}(\boldsymbol{q})\right)^2}{\sigma_{\mathrm{P}}^2} + \dfrac{\left(\tilde{\psi}_{\mathrm{R},k} - \psi_{\mathrm{R},k}(\boldsymbol{q})\right)^2}{\sigma_{\psi}^2} & \text{System 2,} \end{cases} \tag{44}$$

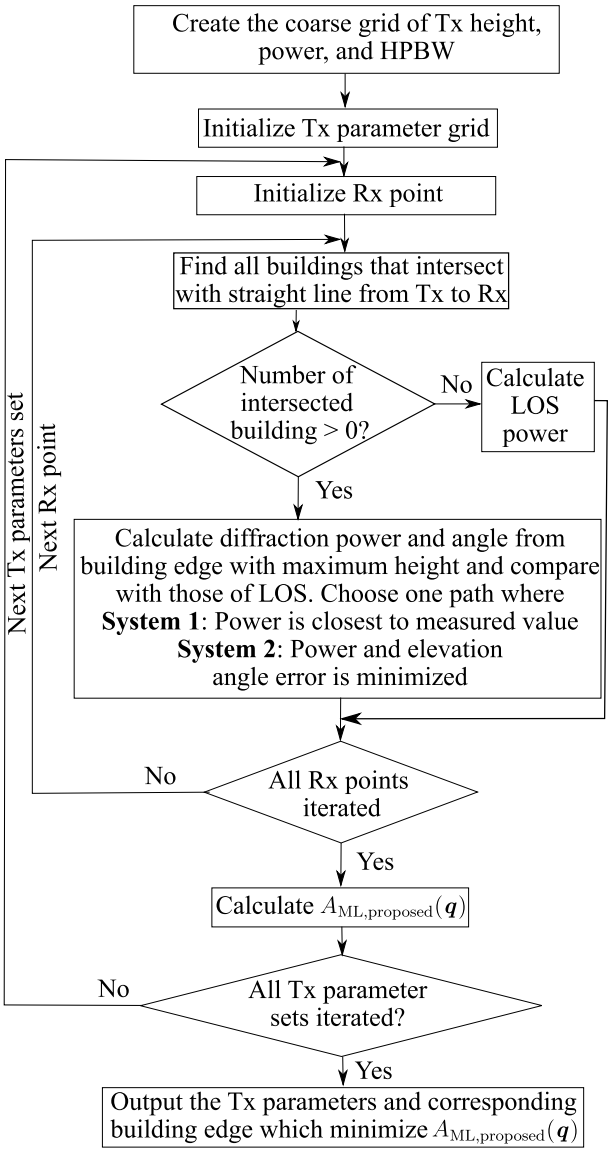

FIGURE 4. Flow chart of coarse search and edge detection.

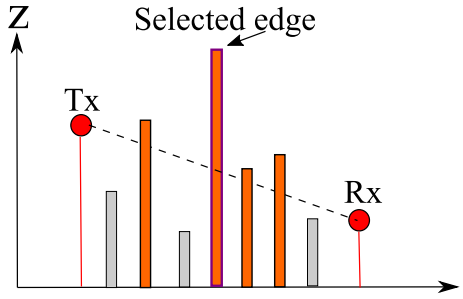

FIGURE 5. Illustration of diffraction edge selection.

where $P_{\mathrm{R},k}(\boldsymbol{q})$ and $\psi_{\mathrm{R},k}(\boldsymbol{q})$ are the received power and elevation angle calculated from either diffraction path or LOS path.

After these steps are calculated for all the Rx points, the ML cost function $A_{\mathrm{ML,proposed}}(\boldsymbol{q})$ is calculated based on (31). The above-mentioned steps are repeated for every possible sets of Tx parameters. Finally, the Tx parameters and its corresponding building edges which minimizes $A_{\mathrm{ML,proposed}}(\boldsymbol{q})$ are chosen by

$$\hat{\boldsymbol{q}}_{\mathrm{initial}} = \arg\min_{\boldsymbol{q}} \left(A_{\mathrm{MLE,proposed}}(\boldsymbol{q})\right) \tag{45}$$

$$\hat{\boldsymbol{e}}_{\mathrm{initial},k} = \hat{\boldsymbol{e}}_k(\hat{\boldsymbol{q}}_{\mathrm{initial}}). \tag{46}$$

D. ITERATIVE FINE SEARCH

After the coarse search with edge detection is performed, the LM algorithm [53] is applied, where $\boldsymbol{q}$ is iteratively updated from its previous position for the predetermined number of times. The LM algorithm is expressed by

$$\hat{\boldsymbol{q}}_{i+1} = \hat{\boldsymbol{q}}_i + \gamma \left(\boldsymbol{J}^T(\hat{\boldsymbol{q}}_i)\boldsymbol{K}^{-1}\boldsymbol{J}(\hat{\boldsymbol{q}}_i) + a\boldsymbol{I}\right)^{-1} \times \boldsymbol{J}^T(\hat{\boldsymbol{q}}_i)\boldsymbol{K}^{-1}\left(\tilde{\boldsymbol{z}} - \boldsymbol{z}(\hat{\boldsymbol{q}}_i)\right) \tag{47}$$

where i and γ are the iteration number and step size, respectively. Therefore, $\hat{\boldsymbol{q}}_1 = \hat{\boldsymbol{q}}_{\mathrm{initial}}$. $\boldsymbol{J}(\hat{\boldsymbol{q}}_i)$ is the Jacobian matrix evaluated at $\hat{\boldsymbol{q}}_i$, which is depicted by

$$\boldsymbol{J}(\boldsymbol{q}) = \begin{bmatrix} \frac{\partial \boldsymbol{\phi}_{\mathrm{R}}(\boldsymbol{q})^T}{\partial p_{\mathrm{x}}} & \frac{\partial \boldsymbol{\psi}_{\mathrm{R}}(\boldsymbol{q})^T}{\partial p_{\mathrm{x}}} & \frac{\partial \boldsymbol{P}_{\mathrm{R}}(\boldsymbol{q})^T}{\partial p_{\mathrm{x}}} \\ \frac{\partial \boldsymbol{\phi}_{\mathrm{R}}(\boldsymbol{q})^T}{\partial p_{\mathrm{y}}} & \frac{\partial \boldsymbol{\psi}_{\mathrm{R}}(\boldsymbol{q})^T}{\partial p_{\mathrm{y}}} & \frac{\partial \boldsymbol{P}_{\mathrm{R}}(\boldsymbol{q})^T}{\partial p_{\mathrm{y}}} \\ \frac{\partial \boldsymbol{\phi}_{\mathrm{R}}(\boldsymbol{q})^T}{\partial p_{\mathrm{z}}} & \frac{\partial \boldsymbol{\psi}_{\mathrm{R}}(\boldsymbol{q})^T}{\partial p_{\mathrm{z}}} & \frac{\partial \boldsymbol{P}_{\mathrm{R}}(\boldsymbol{q})^T}{\partial p_{\mathrm{z}}} \\ \frac{\partial \boldsymbol{\phi}_{\mathrm{R}}(\boldsymbol{q})^T}{\partial \phi_{\mathrm{Tx}}} & \frac{\partial \boldsymbol{\psi}_{\mathrm{R}}(\boldsymbol{q})^T}{\partial \phi_{\mathrm{Tx}}} & \frac{\partial \boldsymbol{P}_{\mathrm{R}}(\boldsymbol{q})^T}{\partial \phi_{\mathrm{Tx}}} \\ \frac{\partial \boldsymbol{\phi}_{\mathrm{R}}(\boldsymbol{q})^T}{\partial \psi_{\mathrm{Tx}}} & \frac{\partial \boldsymbol{\psi}_{\mathrm{R}}(\boldsymbol{q})^T}{\partial \psi_{\mathrm{Tx}}} & \frac{\partial \boldsymbol{P}_{\mathrm{R}}(\boldsymbol{q})^T}{\partial \psi_{\mathrm{Tx}}} \\ \frac{\partial \boldsymbol{\phi}_{\mathrm{R}}(\boldsymbol{q})^T}{\partial P_{\mathrm{T}}} & \frac{\partial \boldsymbol{\psi}_{\mathrm{R}}(\boldsymbol{q})^T}{\partial P_{\mathrm{T}}} & \frac{\partial \boldsymbol{P}_{\mathrm{R}}(\boldsymbol{q})^T}{\partial P_{\mathrm{T}}} \\ \frac{\partial \boldsymbol{\phi}_{\mathrm{R}}(\boldsymbol{q})^T}{\partial \phi_{\mathrm{HPBW}}} & \frac{\partial \boldsymbol{\psi}_{\mathrm{R}}(\boldsymbol{q})^T}{\partial \phi_{\mathrm{HPBW}}} & \frac{\partial \boldsymbol{P}_{\mathrm{R}}(\boldsymbol{q})^T}{\partial \phi_{\mathrm{HPBW}}} \end{bmatrix}^T \tag{48}$$

The derivation of each element of the Jacobian matrix is provided in the Appendix C. It is also to be noted that, for the sake of simplicity, the estimated edge of each Rx position $\hat{\boldsymbol{e}}_{\mathrm{initial},k}$ is assumed to be unchanged for each iteration of the fine search.

III. MEASUREMENT IN THE SUB-URBAN ENVIRONMENT AND DATA ANALYSIS PARAMETERS

To validate the proposed localization method, the measurement campaign was conducted in the sub-urban environment in the Kanto region of Japan. The specifications of the transceivers are given in Table 3. The transmitter is a commercial fixed wireless station operating at the center frequency of 26 GHz. It is mounted at 40 m height above the ground. Two receivers were utilized as shown in Fig. 6. System 1 was the 16 × 2 fan-beam array antenna mounted on the stepping motor. It has a HPBW of 4.5 and 30 degrees in the horizontal and vertical plane, respectively. The motor rotated the antenna from one position to the next in azimuth direction with a precise 3.6 angular step. At each position, the signal was measured by the hand-held spectrum analyzer (R&S FPH26) with the resolution bandwidth of 1 MHz. Furthermore, the 22 dBi gain low noise amplifier (LNA) was connected to increase the received signal power. In the case of system 2, 16 × 16 pencil-beam array antenna was mounted on the 3D rotation system. It has a HPBW of 4.5 degrees.

TABLE 3. Transceiver specifications.

Transmitter	
Frequency	26 GHz band
Height	40 m
System 1	
Antenna array	16 x 2 rectangular array
HPBW	4.5 deg (H), 30 deg (V)
Azimuth step	3.6 deg
bandwidth	1 MHz
LNA gain	22 dBi
Height above ground	2 m
System 2	
Antenna array	16 x 16 rectangular array
HPBW	4.5 deg (H and V)
Azimuth step	∼2.8 deg
Elevation step	4.5 deg
bandwidth	120 kHz
LNA gain	40 dBi
Height above ground	1.5 m

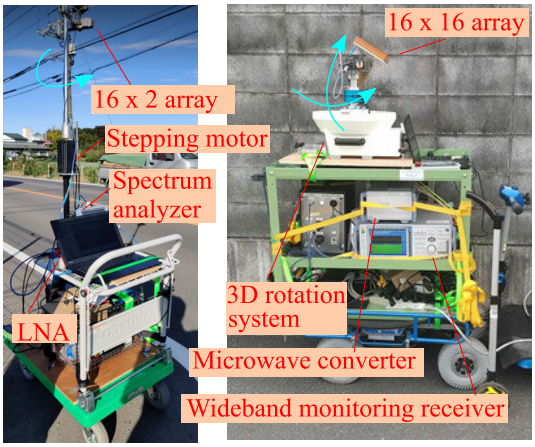

FIGURE 6. Receiver systems ((a) System 1, (b) System 2).

The signal was measured continuously using the wideband monitoring receiver (R&S ESME) and microwave converter (R&S MC40) with the demodulation bandwidth of 120 kHz. The azimuth step was approximately 2.8 degrees. In the elevation direction, the precise 4.5 degree step was used. Moreover, the 40 dBi gain LNA was connected to amplify the received power. Antennas of systems 1 and 2 were mounted at the height of 2 and 1.5 m, respectively

Fig. 7 shows the Tx position, and Rx routes. The measurement site was a sub-urban hilly terrain environment that mostly contains 2 to 3 story residential houses. The Tx was on the base station with a height of 40 m above ground and its main was pointed toward the southeast direction. The Rx was moved on the streets and the signal was measured with 50 m interval. The total number of measurements points were 235 and the measurement was repeated three times at each Rx position. Note that the positions significantly outside the main beam were not measured as the signal power was below the noise level. Moreover, the environment map could not be

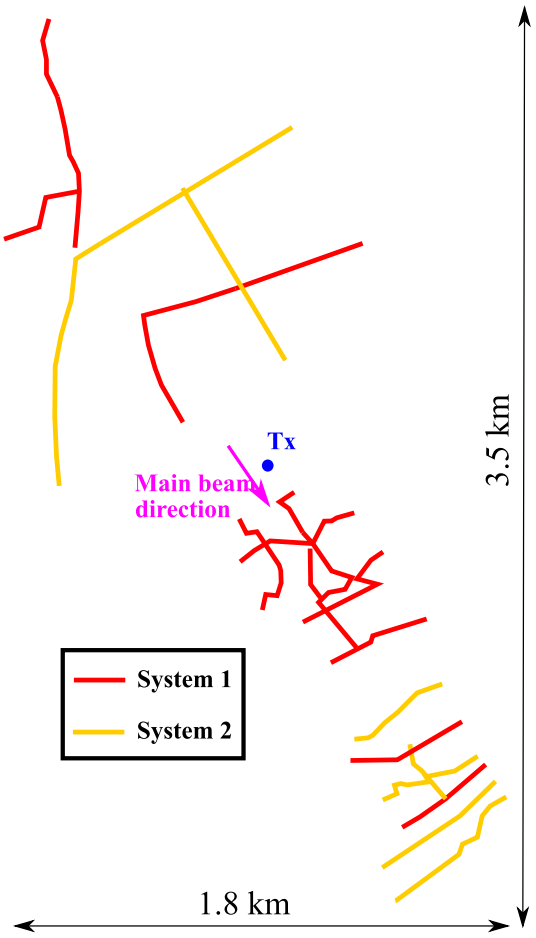

FIGURE 7. Tx position and Rx routes.

TABLE 4. Data analysis parameters.

Parameters	Values
Map database	Zenrin [61]
Dynamic range threshold	10 dB
δ_ϕ	20 deg
N_{Rx}	40, 30, 20
Number of Monte-Carlo trials	500
Noise standard deviation	
σ_{P}	7 dBm
σ_ϕ	5 deg
σ_ψ	4 deg
Coarse search range parameters	
Initial horizontal position $(p_{\mathrm{x}}, p_{\mathrm{y}})$	$\hat{\boldsymbol{p}}_{\mathrm{initial,MLE}}(1:2)$
Vertical position (p_{z})	Terrain height + [5:10:95] m
Transmit power (P_{T})	20:5:40 dBm
HPBW (ϕ_{HPBW})	5:1:7 deg
Fine search parameters	
Number of iteration	200
γ	0.01
a	0.1

shown as it is considered as the confidential information by the operator.

In the data analysis, the proposed MLE and conventional MLE [47], [48] (see Appendix B) were applied to the measurement data. Table 4 provides the parameters. To ensure

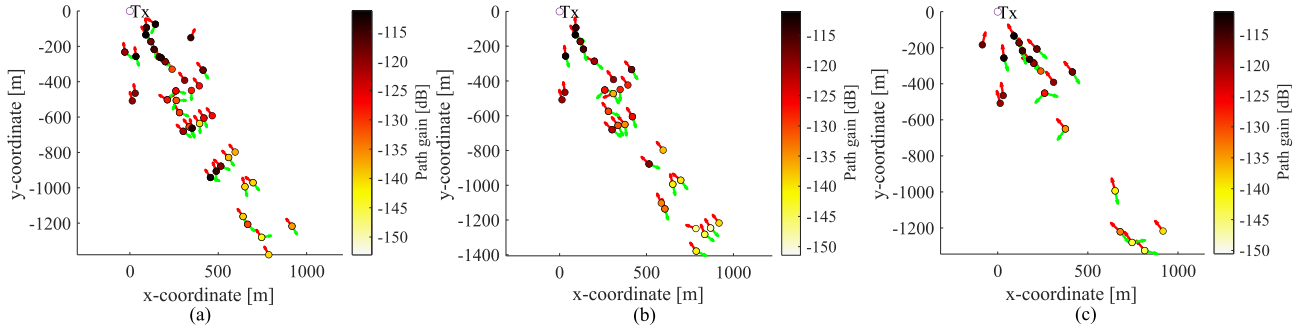

FIGURE 8. Peak identification and clustering results ((a) $N_{Rx} = 40$, (b) $N_{Rx} = 30$, (c) $N_{Rx} = 20$). The red and green arrows represent the two peaks that are categorized into two different clusters.

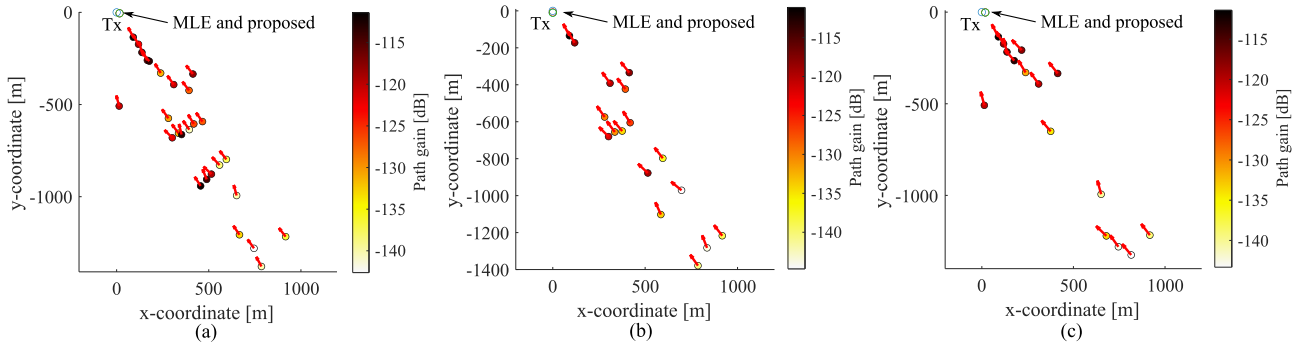

FIGURE 9. Rx points after outlier removal and the estimated position ((a) $N_{Rx} = 40$, (b) $N_{Rx} = 30$, (c) $N_{Rx} = 20$).

sufficient accuracy, only the points where the maximum received power was at least 10 dB above the noise floor were included in the analysis, where there were roughly 50 points that satisfy this criteria. During the analysis, the positions of building edges are determined from the Zenrin map database [61]. In Zenrin map database, building heights from sea level are determined from the topographical data released by Geospatial Information Authority of Japan, and their 3D shapes are constructed from their 2D shapes and number of floors information. In other words, buildings are modeled as irregular prisms with constant horizontal cross sections. Furthermore, the localization was run for 500 trials to statistically see the overall performance of the localization methods. The randomness for each run or sample was generated by uniformly choosing $N_{Rx} = \{40, 30, 20\}$ out of 50 Rx points for the localization. For each Rx point, one out of three measurement repetitions were also chosen randomly.

IV. RESULTS AND DISCUSSION

A. PATH DETECTION AND MECHANISM IDENTIFICATION

Fig. 8 illustrates the peak identification and KPowerMeans clustering results on the map of the first sample for different number of Rx points. The circle marker represents Rx points in which its face color depicts the maximum path gain. The red and green arrows represent the two peaks that are categorized into two different clusters. As expected, these two peaks mostly correspond to LOS, diffraction, or backscattering. Thus, when applying the clustering algorithm using the estimated angle, LOS/diffraction and backscattering clusters could be clearly distinguished in both measurement and RT cases regardless of the number of Rx points. Though, as seen from the plot, some outliers remain, which are thought to be due to the horizontal scattering rather than LOS/diffraction. Thus, the outlier removal as explained in Section II-C has to be applied.

B. VALIDATION OF LOCALIZATION ACCURACY AND COMPARISON WITH THE CONVENTIONAL METHODS

Fig. 9 depicts the Rx points after the LOS/diffraction cluster extraction and outlier removal, and the estimated position using conventional MLE, and the proposed method. It could be seen that the LOS/diffraction clusters were correctly extracted irrespective of the number of Rx points. Furthermore, outliers that correspond to horizontal scattering could be mostly removed. Figs. 10 (a) and (b) show the CDF plot of the horizontal distance and height error for all 500 Monte-Carlo trials. From these results, three important points could be discussed. First of all, in terms of 90th percentile, the horizontal distance error of MLE and the proposed method was comparable for both cases with around 42 m error for the case of $N_{Rx} = 40$, implying that the horizontal position had reached convergence via the conventional MLE. In contrast, the height error had significantly improved from more than 200 m for the conventional MLE, to 45 m for the proposed method. The reason was that there were few Rx points from the measured data where the steep diffraction with a large elevation angle occurred from the houses with triangular roof shapes. Since the conventional MLE interpreted them as LOS

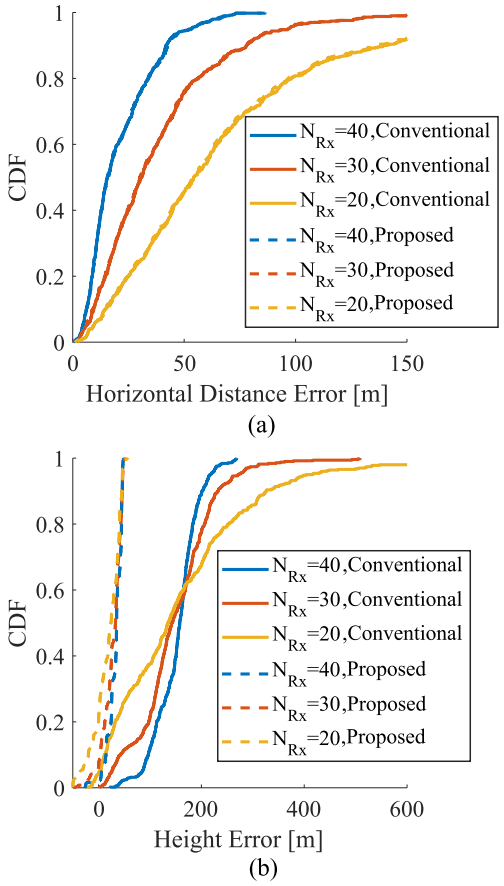

FIGURE 10. Distance error of the proposed and conventional MLE ((a) Horizontal distance error, (b) Height error (predicted value - actual value)).

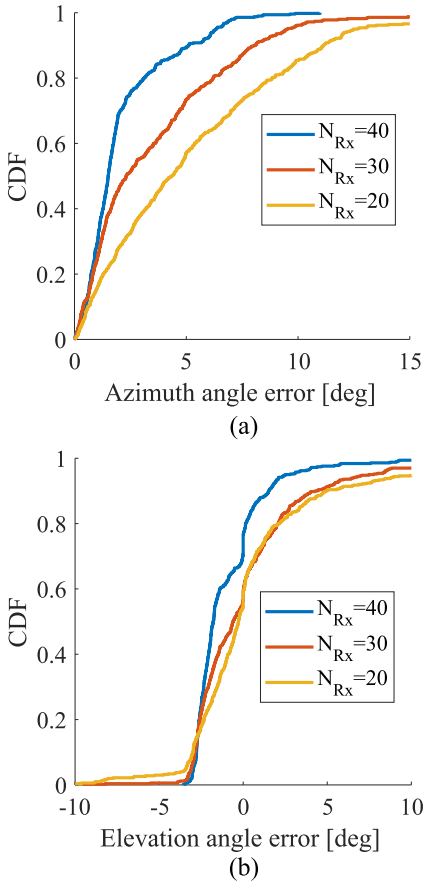

FIGURE 11. Tx angle error of the proposed method ((a) Azimuth, (b) Elevation (predicted value - actual value)).

paths, the Tx height was estimated to be much larger as it tried to compensate for the error caused by these steep diffraction angles. On the contrary, these paths were correctly detected as diffraction in the proposed method; thus, the Tx height overestimation did not occur. Secondly, the standard deviation of the height error of the conventional MLE was inversely proportional to N_{Rx}. This is because those few Rx points with steep diffraction could be better compensated by other Rx points with small elevation angles when N_{Rx} was large. However, in the case of the proposed method, the standard deviation was relatively smaller and was almost independent of N_{Rx} since the diffraction was taken into account. Finally, the horizontal position detection accuracy was proportional to N_{Rx}. This may be due to the few remaining Rx points with horizontal scattering paths which are more likely to cause erroneous results at small N_{Rx}.

C. VALIDATION OF TX DIRECTION AND ANTENNA PATTERN ESTIMATION ACCURACY

Fig. 11 illustrates the CDF plot of the Tx orientation error of the proposed method. Similar to the distance error case, the angle was better predicted at larger N_{Rx}, where the absolute azimuth and elevation errors at $N_{\mathrm{Rx}} = 40$ was smaller than 5 and 3 deg, respectively, for 90% of the time. This indicated that the proposed method could estimate the Tx direction accurately given that the number of receiver points are sufficient.

Furthermore, Fig. 12 depicts the antenna pattern estimation performance in terms of normalized equivalent isotropically radiated power (EIRP) at different Monte-Carlo trials. The normalized EIRP is defined as the ratio between the EIRP estimated from the MLE and the maximum actual EIRP of the Tx antenna. As expected, the results showed that the antenna EIRP accuracy increased with the increase of N_{Rx} as the fluctuation of the results over different Monte-Carlo trials became smaller. Nevertheless, even at $N_{\mathrm{Rx}} = 40$, the HPBW was slightly smaller than the actual HPBW. These inaccuracies might be caused by the received power discrepancies between the calculated and measured values as the actual measurement environment and the Zenrin map database were different. In particular, the shadowing caused by trees, electrical poles, and small objects were not included in the calculation. Another reason is that actual buildings have complex shapes, whereas the building shapes in Zenrin are assumed to be irregular prisms. Moreover, the heights of those buildings are determined from the floor number information, rather than the actual heights, which may caused height inaccuracies. Thus, it might be possible to improve

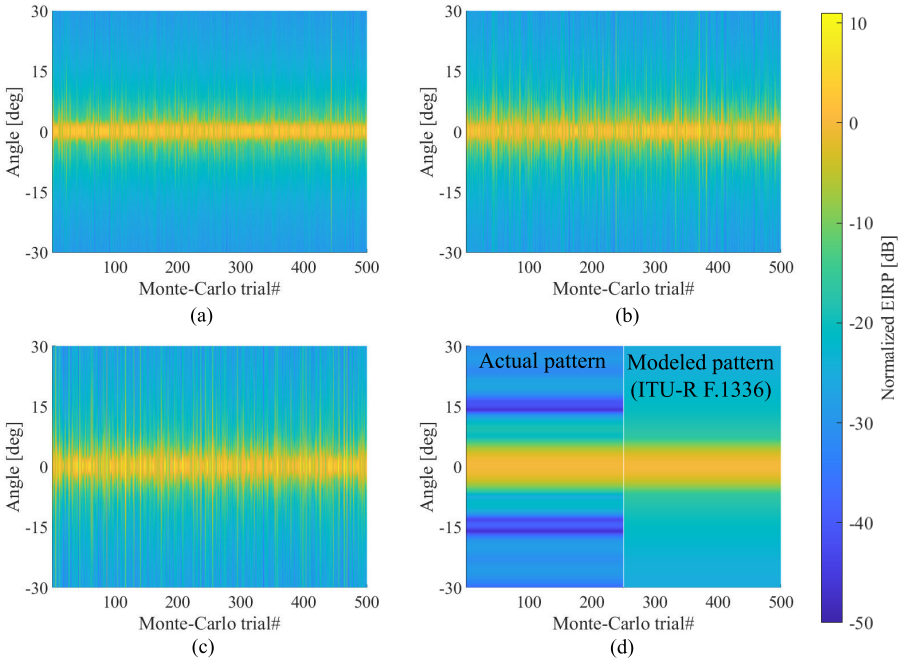

FIGURE 12. EIRP of the Tx antenna ((a) $N_{Rx} = 40$, (b) $N_{Rx} = 30$, (c) $N_{Rx} = 20$, (d) Actual pattern and modeled pattern using ITU-R F.1336 model).

the EIRP prediction accuracy via improving the details of the map database.

V. CONCLUSION

In conclusion, the ML-based transmitter location, direction, power, and antenna pattern estimation method for spectrum sharing at the 26 GHz band had been introduced. This method optimized the joint PDF of the received azimuth angle, elevation angle, and power, which was either calculated by the free space for the LOS or UTD for the diffraction. It was applied to the measured data and compared with the conventional MLE. Three significant conclusions can be drawn. Firstly, the proposed method mostly improved the localization accuracy in the vertical direction in comparison to the conventional MLE, whereas their performances in the horizontal direction were indistinguishable. Secondly, the Tx direction could be accurately estimated if the number of receiver points are sufficient. Finally, the algorithm could roughly predict the antenna envelope pattern with somewhat narrower HPBW due to the difference between the Zenrin database and the actual environment. Nevertheless, these analyses implied that this algorithm should be applicable for localizing and estimating the sharable area of the fixed system operating at the high place in the millimeter-wave bands.

APPENDIX

A. CONVENTIONAL PSEUDOLINEAR ESTIMATOR

In the PLE [47], [48], the 2D location of emitter could be estimated from least squares by

$$\begin{bmatrix} \hat{p}_x \\ \hat{p}_y \end{bmatrix} = \left(\boldsymbol{A}^T\boldsymbol{A}\right)^{-1}\boldsymbol{A}^T\boldsymbol{b} \tag{49}$$

where

$$\boldsymbol{A} = \begin{bmatrix} \sin\tilde{\phi}_{R,1} & -\cos\tilde{\phi}_{R,1} \\ \vdots & \vdots \\ \sin\tilde{\phi}_{R,N} & -\cos\tilde{\phi}_{R,N} \end{bmatrix} \tag{50}$$

$$\begin{bmatrix} r_x(1)\sin\tilde{\phi}_{R,1} - r_y(1)\cos\tilde{\phi}_{R,1} \\ \vdots \\ r_x(N)\sin\tilde{\phi}_{R,N} - r_y(N)\cos\tilde{\phi}_{R,N} \end{bmatrix} \tag{51}$$

Then, the z-coordinate of the emitter is found by

$$\hat{p}_z = \frac{1}{N_2}\sum_{k=1}^{N_2}\left(r_{z,k} + \left\|\begin{bmatrix} p_x - r_{x,k} \\ p_y - r_{y,k} \end{bmatrix}\right\| \tan\tilde{\psi}_{R,k}\right) \tag{52}$$

Notice that both system 1 and system 2 were used to calculate (49), while only system 2 were exploited to compute (52).

B. CONVENTIONAL MAXIMUM LIKELIHOOD ESTIMATOR

In the conventional MLE [47], [48], the total signal model is constructed by

$$\tilde{\boldsymbol{y}} = \boldsymbol{y}(\boldsymbol{p}) + \boldsymbol{w}_2 \tag{53}$$

$$\tilde{\boldsymbol{y}} = \left[\tilde{\boldsymbol{\phi}}_R, \tilde{\boldsymbol{\psi}}_R\right]^T \tag{54}$$

$$\boldsymbol{y}(\boldsymbol{p}) = \left[\boldsymbol{\phi}_R(\boldsymbol{p}), \boldsymbol{\psi}_R(\boldsymbol{p})\right]^T \tag{55}$$

$$\boldsymbol{w}_2 = \left[\boldsymbol{w}_\phi, \boldsymbol{w}_\psi\right]^T \tag{56}$$

Assuming that $\boldsymbol{K}_2 = \text{diag}\left(\sigma_\phi^2, .., \sigma_\phi^2, \sigma_\psi^2, \ldots, \sigma_\psi^2\right)$, the MLE could be derived by

$$A_{ML}(\boldsymbol{p}) = [\tilde{\boldsymbol{y}} - \boldsymbol{y}(\boldsymbol{p})]^T\boldsymbol{K}_2^{-1}[\tilde{\boldsymbol{y}} - \boldsymbol{y}(\boldsymbol{p})] \tag{57}$$

$$\hat{\boldsymbol{p}}_{MLE} = \arg\min(A_{ML}(\boldsymbol{p})) \tag{58}$$

C. JACOBIAN MATRIX DERIVATION

The Jacobian matrix is calculated by

$$\boldsymbol{J}(\boldsymbol{q}) = \begin{bmatrix} \frac{\partial \boldsymbol{\phi}_{\mathrm{R}}(\boldsymbol{q})^T}{\partial p_{\mathrm{x}}} & \frac{\partial \boldsymbol{\psi}_{\mathrm{R}}(\boldsymbol{q})^T}{\partial p_{\mathrm{x}}} & \frac{\partial \boldsymbol{P}_{\mathrm{R}}(\boldsymbol{q})^T}{\partial p_{\mathrm{x}}} \\ \frac{\partial \boldsymbol{\phi}_{\mathrm{R}}(\boldsymbol{q})^T}{\partial p_{\mathrm{y}}} & \frac{\partial \boldsymbol{\psi}_{\mathrm{R}}(\boldsymbol{q})^T}{\partial p_{\mathrm{y}}} & \frac{\partial \boldsymbol{P}_{\mathrm{R}}(\boldsymbol{q})^T}{\partial p_{\mathrm{y}}} \\ \frac{\partial \boldsymbol{\phi}_{\mathrm{R}}(\boldsymbol{q})^T}{\partial p_{\mathrm{z}}} & \frac{\partial \boldsymbol{\psi}_{\mathrm{R}}(\boldsymbol{q})^T}{\partial p_{\mathrm{z}}} & \frac{\partial \boldsymbol{P}_{\mathrm{R}}(\boldsymbol{q})^T}{\partial p_{\mathrm{z}}} \\ \frac{\partial \boldsymbol{\phi}_{\mathrm{R}}(\boldsymbol{q})^T}{\partial \phi_{\mathrm{Tx}}} & \frac{\partial \boldsymbol{\psi}_{\mathrm{R}}(\boldsymbol{q})^T}{\partial \phi_{\mathrm{Tx}}} & \frac{\partial \boldsymbol{P}_{\mathrm{R}}(\boldsymbol{q})^T}{\partial \phi_{\mathrm{Tx}}} \\ \frac{\partial \boldsymbol{\phi}_{\mathrm{R}}(\boldsymbol{q})^T}{\partial \psi_{\mathrm{Tx}}} & \frac{\partial \boldsymbol{\psi}_{\mathrm{R}}(\boldsymbol{q})^T}{\partial \psi_{\mathrm{Tx}}} & \frac{\partial \boldsymbol{P}_{\mathrm{R}}(\boldsymbol{q})^T}{\partial \psi_{\mathrm{Tx}}} \\ \frac{\partial \boldsymbol{\phi}_{\mathrm{R}}(\boldsymbol{q})^T}{\partial P_{\mathrm{T}}} & \frac{\partial \boldsymbol{\psi}_{\mathrm{R}}(\boldsymbol{q})^T}{\partial P_{\mathrm{T}}} & \frac{\partial \boldsymbol{P}_{\mathrm{R}}(\boldsymbol{q})^T}{\partial P_{\mathrm{T}}} \\ \frac{\partial \boldsymbol{\phi}_{\mathrm{R}}(\boldsymbol{q})^T}{\partial \phi_{\mathrm{HPBW}}} & \frac{\partial \boldsymbol{\psi}_{\mathrm{R}}(\boldsymbol{q})^T}{\partial \phi_{\mathrm{HPBW}}} & \frac{\partial \boldsymbol{P}_{\mathrm{R}}(\boldsymbol{q})^T}{\partial \phi_{\mathrm{HPBW}}} \end{bmatrix}^T \tag{59}$$

Note that throughout this section, angles have the unit of radian. Powers and antenna patterns have the unit of dB. Based on the conventional method [47], [48], the derivative of the azimuth and elevation angle of arrivals with respect to position are expressed by

$$\frac{\partial \phi_{\mathrm{R},k}(\boldsymbol{q})}{\partial p_{\mathrm{x}}} = -\frac{\sin\left(\phi_{\mathrm{R},k}(\boldsymbol{q})\right)}{\sqrt{(p_{\mathrm{x}} - r_{\mathrm{x},k})^2 + (p_{\mathrm{y}} - r_{\mathrm{y},k})^2}} \tag{60}$$

$$\frac{\partial \phi_{\mathrm{R},k}(\boldsymbol{q})}{\partial p_{\mathrm{y}}} = \frac{\cos\left(\phi_{\mathrm{R},k}(\boldsymbol{q})\right)}{\sqrt{(p_{\mathrm{x}} - r_{\mathrm{x},k})^2 + (p_{\mathrm{y}} - r_{\mathrm{y},k})^2}} \tag{61}$$

$$\frac{\partial \phi_{\mathrm{R},k}(\boldsymbol{q})}{\partial p_{\mathrm{z}}} = 0 \tag{62}$$

$$\frac{\partial \psi_{\mathrm{R},k}(\boldsymbol{q})}{\partial p_{\mathrm{x}}} = -\frac{\sin\psi_{\mathrm{R},k}(\boldsymbol{q})\cos\phi_{\mathrm{R},k}(\boldsymbol{q})}{\|\boldsymbol{p} - \boldsymbol{r}_k\|} \tag{63}$$

$$\frac{\partial \psi_{\mathrm{R},k}(\boldsymbol{q})}{\partial p_{\mathrm{y}}} = -\frac{\sin\psi_{\mathrm{R},k}(\boldsymbol{q})\sin\phi_{\mathrm{R},k}(\boldsymbol{q})}{\|\boldsymbol{p} - \boldsymbol{r}_k\|} \tag{64}$$

$$\frac{\partial \psi_{\mathrm{R},k}(\boldsymbol{q})}{\partial p_{\mathrm{z}}} = \frac{\cos^2\psi_{\mathrm{R},k}(\boldsymbol{q})}{\sqrt{(p_{\mathrm{x}} - r_{\mathrm{x},k})^2 + (p_{\mathrm{y}} - r_{\mathrm{y},k})^2}} \tag{65}$$

Note that in case of diffraction, the derivative of $\psi_{\mathrm{R},k}(\boldsymbol{q})$ is zero as it is assumed that the edge position does not change after the coarse search. In the case of $\phi_{\mathrm{R},k}(\boldsymbol{q})$, the derivative follows the LOS case.

Then, the derivative of the azimuth and elevation angle of arrivals with respect to Tx direction, HPBW and antenna pattern slope are zero as they are independent of each other.

The derivative of the received power with respect to the transmit power is one.

$$\frac{\partial P_{\mathrm{R},k}(\boldsymbol{q})}{\partial P_{\mathrm{T}}} = 1 \tag{66}$$

The derivative of the received power with respect to ϕ_{HPBW}, ϕ_{Tx}, ψ_{Tx} are as follows

$$\frac{\partial P_{\mathrm{R},k}(\boldsymbol{q})}{\partial \phi_{\mathrm{HPBW}}} = \begin{cases} 24x\frac{\cos^{-1}(\cos\phi'_k\cos\psi'_k)}{\phi^2_{\mathrm{HPBW}}} & x < 1.152 \\ \frac{15\log_{10}(e)}{x}\cdot\frac{\cos^{-1}(\cos\phi'_k\cos\psi'_k)}{\phi^2_{\mathrm{HPBW}}} & x \geq 1.152 \end{cases} \tag{67}$$

$$\frac{\partial P_{\mathrm{R},k}(\boldsymbol{q})}{\partial \phi_{\mathrm{Tx}}} = \begin{cases} \frac{24x}{\sqrt{1-\cos^2\phi'_k\cos^2\psi'_k}}\sin\phi'_k\cos\psi'_k & x < 1.152 \\ \frac{15\log_{10}(e)}{x\sqrt{1-\cos^2\phi'_k\cos^2\psi'_k}}\sin\phi'_k\cos\psi'_k & x \geq 1.152 \end{cases} \tag{68}$$

$$\frac{\partial P_{\mathrm{R},k}(\boldsymbol{q})}{\partial \psi_{\mathrm{Tx}}} = \begin{cases} \frac{24x}{\sqrt{1-\cos^2\phi'_k\cos^2\psi'_k}}\cos\phi'_k\sin\psi'_k & x < 1.152 \\ \frac{15\log_{10}(e)}{x\sqrt{1-\cos^2\phi'_k\cos^2\psi'_k}}\cos\phi'_k\sin\psi'_k & x \geq 1.152 \end{cases} \tag{69}$$

where $\phi'_k = \phi_{\mathrm{T},k}(\boldsymbol{q}) - \phi_{\mathrm{Tx}}$ and $\psi'_k = \psi_{\mathrm{T},k}(\boldsymbol{q}) - \psi_{\mathrm{Tx}}$. x is expressed by (2)

The derivative of received power with respect to p_{x}, p_{y}, and p_{z} of the first system is expressed by

$$\frac{\partial P_{\mathrm{R},k}(\boldsymbol{q})}{\partial p_{\mathrm{x}}} = \frac{\partial G_{\mathrm{Tx}}(\phi_{\mathrm{HPBW}}, \phi'_k, \psi'_k)}{\partial p_{\mathrm{x}}} + \frac{\partial L_{\mathrm{p},k}(\boldsymbol{q})}{\partial p_{\mathrm{x}}} + G'_{\mathrm{Rx},1}(\psi_{\mathrm{R},k}(\boldsymbol{q}))\frac{\partial \psi_{\mathrm{R},k}(\boldsymbol{q})}{\partial p_{\mathrm{x}}} \tag{70}$$

$$\frac{\partial P_{\mathrm{R},k}(\boldsymbol{q})}{\partial p_{\mathrm{y}}} = \frac{\partial G_{\mathrm{Tx}}(\phi_{\mathrm{HPBW}}, \phi'_k, \psi'_k)}{\partial p_{\mathrm{y}}} + \frac{\partial L_{\mathrm{p},k}(\boldsymbol{q})}{\partial p_{\mathrm{y}}} + G'_{\mathrm{Rx},1}(\psi_{\mathrm{R},k}(\boldsymbol{q}))\frac{\partial \psi_{\mathrm{R},k}(\boldsymbol{q})}{\partial p_{\mathrm{y}}} \tag{71}$$

$$\frac{\partial P_{\mathrm{R},k}(\boldsymbol{q})}{\partial p_{\mathrm{z}}} = \frac{\partial G_{\mathrm{Tx}}(\phi_{\mathrm{HPBW}}, \phi'_k, \psi'_k)}{\partial p_{\mathrm{z}}} + \frac{\partial L_{\mathrm{p},k}(\boldsymbol{q})}{\partial p_{\mathrm{z}}} + G'_{\mathrm{Rx},1}(\psi_{\mathrm{R},k}(\boldsymbol{q}))\frac{\partial \psi_{\mathrm{R},k}(\boldsymbol{q})}{\partial p_{\mathrm{z}}} \tag{72}$$

Note that for system 2, the last term of (70), (71), and (72) are zero, since the antenna gain is assumed constant. For the first system, the derivative of antenna pattern in dB with respect to the elevation angle could be calculated by

$$G'_{\mathrm{Rx},1}(\psi_{\mathrm{R},k}(\boldsymbol{q})) = \frac{G_{\mathrm{Rx},1}(\psi_{\mathrm{R},k}(\boldsymbol{q}) + \Delta\psi) - G_{\mathrm{Rx},1}(\psi_{\mathrm{R},k}(\boldsymbol{q}))}{\Delta\psi} \tag{73}$$

where $\Delta\psi$ is a small angular step.

The partial derivative of the antenna pattern is expressed by

$$\frac{\partial G_{\mathrm{Tx}}(\phi_{\mathrm{HPBW}}, \phi'_k, \psi'_k)}{\partial p_{\mathrm{x}}} = -\frac{\partial P_{\mathrm{R},k}(\boldsymbol{q})}{\partial \phi_{\mathrm{Tx}}}\frac{\partial \phi_{\mathrm{T},k}(\boldsymbol{q})}{\partial p_{\mathrm{x}}} - \frac{\partial P_{\mathrm{R},k}(\boldsymbol{q})}{\partial \psi_{\mathrm{Tx}}}\frac{\partial \psi_{\mathrm{T},k}(\boldsymbol{q})}{\partial p_{\mathrm{x}}} \tag{74}$$

$$\frac{\partial G_{\mathrm{Tx}}(\phi_{\mathrm{HPBW}}, \phi'_k, \psi'_k)}{\partial p_{\mathrm{y}}} = -\frac{\partial P_{\mathrm{R},k}(\boldsymbol{q})}{\partial \phi_{\mathrm{Tx}}}\frac{\partial \phi_{\mathrm{T},k}(\boldsymbol{q})}{\partial p_{\mathrm{y}}} - \frac{\partial P_{\mathrm{R},k}(\boldsymbol{q})}{\partial \psi_{\mathrm{Tx}}}\frac{\partial \psi_{\mathrm{T},k}(\boldsymbol{q})}{\partial p_{\mathrm{y}}} \tag{75}$$

$$\frac{\partial G_{\mathrm{Tx}}(\phi_{\mathrm{HPBW}}, \phi'_k, \psi'_k)}{\partial p_{\mathrm{z}}} = -\frac{\partial P_{\mathrm{R},k}(\boldsymbol{q})}{\partial \phi_{\mathrm{Tx}}}\frac{\partial \phi_{\mathrm{T},k}(\boldsymbol{q})}{\partial p_{\mathrm{z}}} - \frac{\partial P_{\mathrm{R},k}(\boldsymbol{q})}{\partial \psi_{\mathrm{Tx}}}\frac{\partial \psi_{\mathrm{T},k}(\boldsymbol{q})}{\partial p_{\mathrm{z}}} \tag{76}$$

$\frac{\partial P_{\mathrm{R},k}(\boldsymbol{q})}{\partial \phi_{\mathrm{Tx}}}$ and $\frac{\partial P_{\mathrm{R},k}(\boldsymbol{q})}{\partial \psi_{\mathrm{Tx}}}$ could be found from (68) and (69). In case of LOS, the derivative of $\phi_{\mathrm{T},k}(\boldsymbol{q})$ and $\psi_{\mathrm{T},k}(\boldsymbol{q})$ could simply be derived from (12) and (13) by

$$\frac{\partial \phi_{\mathrm{T},k}(\boldsymbol{q})}{\partial p} = \frac{\partial \phi_{\mathrm{R},k}(\boldsymbol{q})}{\partial p} \tag{77}$$

$$\frac{\partial \psi_{\mathrm{T},k}(\boldsymbol{q})}{\partial p} = -\frac{\partial \psi_{\mathrm{R},k}(\boldsymbol{q})}{\partial p} \tag{78}$$

where $p \in \{p_x, p_y, p_z\}$. In case of diffraction, the derivative is derived from (14) and (15) by

$$\frac{\partial \phi_{T,k}(\boldsymbol{q})}{\partial p_x} = -\frac{\sin\left(\phi_{T,k}(\boldsymbol{q})\right)}{\sqrt{(p_x - e_{x,k})^2 + (p_y - e_{y,k})^2}} \tag{79}$$

$$\frac{\partial \phi_{T,k}(\boldsymbol{q})}{\partial p_y} = \frac{\cos\left(\phi_{T,k}(\boldsymbol{q})\right)}{\sqrt{(p_x - e_{x,k})^2 + (p_y - e_{y,k})^2}} \tag{80}$$

$$\frac{\partial \phi_{T,k}(\boldsymbol{q})}{\partial p_z} = 0 \tag{81}$$

$$\frac{\partial \psi_{T,k}(\boldsymbol{q})}{\partial p_x} = -\frac{\sin\psi_{T,k}(\boldsymbol{q})\cos\phi_{T,k}(\boldsymbol{q})}{\|\boldsymbol{p} - \boldsymbol{e}_k\|} \tag{82}$$

$$\frac{\partial \psi_{T,k}(\boldsymbol{q})}{\partial p_y} = -\frac{\sin\psi_{T,k}(\boldsymbol{q})\sin\phi_{T,k}(\boldsymbol{q})}{\|\boldsymbol{p} - \boldsymbol{e}_k\|} \tag{83}$$

$$\frac{\partial \psi_{T,k}(\boldsymbol{q})}{\partial p_z} = \frac{\cos^2\psi_{T,k}(\boldsymbol{q})}{\sqrt{(p_x - e_{x,k})^2 + (p_y - e_{y,k})^2}} \tag{84}$$

The derivative of $L_{p,k}(\boldsymbol{q})$ in case of LOS is derived from the free space equation by

$$\frac{\partial L_{p,k}(\boldsymbol{q})}{\partial p_x} = \frac{20}{\|\boldsymbol{p} - \boldsymbol{r}_k\|^2 \ln 10}(p_x - r_{x,k}) \tag{85}$$

$$\frac{\partial L_{p,k}(\boldsymbol{q})}{\partial p_y} = \frac{20}{\|\boldsymbol{p} - \boldsymbol{r}_k\|^2 \ln 10}(p_y - r_{y,k}) \tag{86}$$

$$\frac{\partial L_{p,k}(\boldsymbol{q})}{\partial p_z} = \frac{20}{\|\boldsymbol{p} - \boldsymbol{r}_k\|^2 \ln 10}(p_z - r_{z,k}) \tag{87}$$

The UTD equation (17) could also be expressed by

$$L_{p,k}(\boldsymbol{q}) = 10\log_{10}\left(B_k(\boldsymbol{q})\right) + 10\log_{10}\left(C_k(\boldsymbol{q})\right), \tag{88}$$

where

$$B_k(\boldsymbol{q}) = \frac{1}{\left(s_k'^2(\boldsymbol{q}) + s_k'(\boldsymbol{q})s_k(\boldsymbol{q})\right)\sin^2\left(\frac{\alpha_k(\boldsymbol{q})}{2}\right)}, \tag{89}$$

and

$$C_k(\boldsymbol{q}) = \left|F\left(\frac{4\pi}{\lambda}\frac{s_k'(\boldsymbol{q})s_k(\boldsymbol{q})}{s_k'(\boldsymbol{q}) + s_k(\boldsymbol{q})}\sin^2\left(\frac{\alpha_k(\boldsymbol{q})}{2}\right)\right)\right|^2. \tag{90}$$

Thus, the derivative of (88) is expressed by

$$\frac{\partial L_{p,k}(\boldsymbol{q})}{\partial p} = \frac{10}{\ln 10}\left(\frac{B_k'(\boldsymbol{q})}{B_k(\boldsymbol{q})} + \frac{C_k'(\boldsymbol{q})}{C_k(\boldsymbol{q})}\right) \tag{91}$$

where $p \in \{p_x, p_y, p_z\}$. $B_k'(\boldsymbol{q})$ and $C_k'(\boldsymbol{q})$ are the derivative of $B_k(\boldsymbol{q})$ and $C_k(\boldsymbol{q})$, respectively. Therefore,

$$\begin{aligned} B_k'(\boldsymbol{q}) = &-\left(s_k'^2(\boldsymbol{q}) + s_k'(\boldsymbol{q})s_k(\boldsymbol{q})\right)^{-2}\left(2s_k'(\boldsymbol{q}) + s_k(\boldsymbol{q})\right) \\ &\times \frac{\partial s_k'(\boldsymbol{q})}{\partial p}\sin^{-2}\left(\frac{\alpha_k(\boldsymbol{q})}{2}\right) - \frac{1}{\left(s_k'^2(\boldsymbol{q}) + s_k'(\boldsymbol{q})s_k(\boldsymbol{q})\right)} \\ &\times \sin^{-3}(\alpha_k(\boldsymbol{q})/2)\cos(\alpha_k(\boldsymbol{q})/2)\frac{\partial \phi_k'(\boldsymbol{q})}{\partial p}, \end{aligned} \tag{92}$$

and

$$\begin{aligned} C_k'(\boldsymbol{q}) = 2&\left|F\left(\frac{4\pi}{\lambda}\frac{s_k'(\boldsymbol{q})s_k(\boldsymbol{q})}{s_k'(\boldsymbol{q}) + s_k(\boldsymbol{q})}\sin^2\left(\frac{\alpha_k(\boldsymbol{q})}{2}\right)\right)\right| \\ &\cdot \left|F\left(\frac{4\pi}{\lambda}\frac{s_k'(\boldsymbol{q})s_k(\boldsymbol{q})}{s_k'(\boldsymbol{q}) + s_k(\boldsymbol{q})}\sin^2\left(\frac{\alpha_k(\boldsymbol{q})}{2}\right)\right)\right|' \\ &\cdot \frac{4\pi}{\lambda}s_k(\boldsymbol{q})\left[\frac{\partial s_k'(\boldsymbol{q})}{\partial p}\frac{1}{(s_k'(\boldsymbol{q}) + s_k(\boldsymbol{q}))}\sin^2\left(\frac{\alpha_k(\boldsymbol{q})}{2}\right)\right. \\ &- s_k'(\boldsymbol{q})(s_k'(\boldsymbol{q}) + s_k(\boldsymbol{q}))^{-2}\frac{\partial s_k'(\boldsymbol{q})}{\partial p}\sin^2\left(\frac{\alpha_k(\boldsymbol{q})}{2}\right) \\ &+ s_k'(\boldsymbol{q})(s_k'(\boldsymbol{q}) + s_k(\boldsymbol{q}))^{-1}\sin\left(\frac{\alpha_k(\boldsymbol{q})}{2}\right) \\ &\left.\times \cos\left(\frac{\alpha_k(\boldsymbol{q})}{2}\right)\frac{\partial \phi_k'(\boldsymbol{q})}{\partial p}\right]. \end{aligned} \tag{93}$$

The derivative of Fresnel integral in (93) may be rigorously derived. However, for simplicity, it is approximated using the differential calculus principle.

$$|F(y)|' = \frac{|F(y + \Delta y)| - |F(y)|}{\Delta y} \tag{94}$$

where Δy is a small step, which is set to 0.0001 in this paper.

The derivative of Tx to edge distance with respect to position are

$$\frac{\partial s_k'(\boldsymbol{q})}{\partial p_x} = \frac{p_x - e_{x,k}(\boldsymbol{q})}{\|\boldsymbol{p} - \boldsymbol{e}_k(\boldsymbol{q})\|} \tag{95}$$

$$\frac{\partial s_k'(\boldsymbol{q})}{\partial p_y} = \frac{p_y - e_{y,k}(\boldsymbol{q})}{\|\boldsymbol{p} - \boldsymbol{e}_k(\boldsymbol{q})\|} \tag{96}$$

$$\frac{\partial s_k'(\boldsymbol{q})}{\partial p_z} = \frac{p_z - e_{z,k}(\boldsymbol{q})}{\|\boldsymbol{p} - \boldsymbol{e}_k(\boldsymbol{q})\|} \tag{97}$$

The derivative of $\phi_k'(\boldsymbol{q})$ with respect to position are

$$\frac{\partial \phi_k'(\boldsymbol{q})}{\partial p_x} = \frac{e_{z,k}(\boldsymbol{q}) - p_z}{\sqrt{1 - \left(\frac{\partial s_k'(\boldsymbol{q})}{\partial p_z}\right)^2}} \cdot \frac{p_x - e_{x,k}(\boldsymbol{q})}{\|\boldsymbol{p} - \boldsymbol{e}_k(\boldsymbol{q})\|^3} \tag{98}$$

$$\frac{\partial \phi_k'(\boldsymbol{q})}{\partial p_y} = \frac{e_z(k) - p_z}{\sqrt{1 - \left(\frac{\partial s_k'(\boldsymbol{q})}{\partial p_z}\right)^2}} \cdot \frac{p_y - e_{y,k}(\boldsymbol{q})}{\|\boldsymbol{p} - \boldsymbol{e}_k(\boldsymbol{q})\|^3} \tag{99}$$

$$\begin{aligned} \frac{\partial \phi_k'(\boldsymbol{q})}{\partial p_z} = &\frac{1}{\sqrt{1 - \left(\frac{\partial s_k'(\boldsymbol{q})}{\partial p_z}\right)^2}} \cdot \left[\frac{1}{s_k(\boldsymbol{q})}\right. \\ &\left. - \frac{(e_{z,k}(\boldsymbol{q}) - p_z)^2}{s_k(\boldsymbol{q})^3}\right] \end{aligned} \tag{100}$$

Thus, $C_k'(\boldsymbol{q})$ can be found by substituting (94)-(100) to (93)

REFERENCES

[1] T. S. Rappaport, S. Sun, R. Mayzus, H. Zhao, Y. Azar, K. Wang, G. N. Wong, J. K. Schulz, M. Samimi, and F. Gutierrez, "Millimeter wave mobile communications for 5G cellular: It will work!" *IEEE Access*, vol. 1, pp. 335–349, 2013.

[2] K. Sakaguchi, E. M. Mohamed, H. Kusano, M. Mizukami, S. Miyamoto, R. E. Rezagah, K. Takinami, K. Takahashi, N. Shirakata, H. Peng, T. Yamamoto, and S. Nanba, "Millimeter-wave wireless LAN and its extension toward 5G heterogeneous networks," *IEICE Trans. Commun.*, vol. 98, no. 10, pp. 1932–1948, 2015.

[3] *Fixed Wireless Access System Using Quasi-Millimeter-Wave and Millimeter-Wave-Band Frequencies Point to Point System*, Standard ARIB STD-T58, Oct. 2000.

[4] *Fixed Wireless Access System Using Quasi-Millimeter-Wave and Millimeter-Wave-Band Frequencies Point to Multipoint System*, Standard ARIB STD-T59, Mar. 2000.

[5] *25 GHz Band Low Power Data Communication Device NTG-2501*. Japan Radio. Accessed: Mar. 31, 2021. [Online]. Available: http://www.jrc.co.jp/jp/product/lineup/ntg2501/index.html

[6] K. Murakami, J.-I. Takada, K. Saito, and P. Hanpinitsak, "A Kirchhoff approximation based spectrum availability prediction method at millimeter wave," in *Proc. 14th Eur. Conf. Antennas Propag. (EuCAP)*, Mar. 2020, pp. 1–2.

[7] C. Zhan, H. Gupta, A. Bhattacharya, and M. Ghaderibaneh, "Efficient localization of multiple intruders in shared spectrum system," in *Proc. 19th ACM/IEEE Int. Conf. Inf. Process. Sensor Netw. (IPSN)*, Apr. 2020, pp. 205–216.

[8] C. Zhan, M. Ghaderibaneh, P. Sahu, and H. Gupta, "DeepMTL: Deep learning based multiple transmitter localization," in *Proc. IEEE 22nd Int. Symp. World Wireless, Mobile Multimedia Netw. (WoWMoM)*, Jun. 2021, pp. 41–50.

[9] R. Chen, J. M. Park, and J. H. Reed, "Defense against primary user emulation attacks in cognitive radio networks," *IEEE J. Sel. Areas Commun.*, vol. 26, no. 1, pp. 25–37, Jan. 2008.

[10] A. Dutta and M. Chiang, "'See something, say something' crowdsourced enforcement of spectrum policies," *IEEE Trans. Wireless Commun.*, vol. 15, no. 1, pp. 67–80, Jan. 2016.

[11] K. Tsukamoto, M. Kitsunezuka, and K. Kunihiro, "Highly accurate radio environment mapping method based on transmitter localization and spatial interpolation in urban LoS/NLoS scenario," in *Proc. IEEE Top. Conf. Wireless Sensors Sensor Netw. (WiSNet)*, Jan. 2018, pp. 5–7.

[12] S. Liu, Y. Chen, W. Trappe, and L. J. Greenstein, "Non-interactive localization of cognitive radios based on dynamic signal strength mapping," in *Proc. 6th Int. Conf. Wireless On-Demand Netw. Syst. Services*, Feb. 2009, pp. 85–92.

[13] P. Zhang, J. Lu, Y. Wang, and Q. Wang, "Cooperative localization in 5G networks: A survey," *ICT Exp.*, vol. 3, no. 1, pp. 27–32, Mar. 2017.

[14] F. Wen, H. Wymeersch, B. Peng, W. P. Tay, H. C. So, and D. Yang, "A survey on 5G massive MIMO localization," *Digit. Signal Process.*, vol. 94, pp. 21–28, Nov. 2019.

[15] A. Shahmansoori, G. E. Garcia, G. Destino, G. Seco-Granados, and H. Wymeersch, "Position and orientation estimation through millimeter-wave MIMO in 5G systems," *IEEE Trans. Wireless Commun.*, vol. 17, no. 3, pp. 1822–1835, Mar. 2017.

[16] A. Guerra, F. Guidi, and D. Dardari, "Position and orientation error bound for wideband massive antenna arrays," in *Proc. IEEE Int. Conf. Commun. Workshop (ICCW)*, Jun. 2015, pp. 853–858.

[17] R. Mendrzik, H. Wymeersch, G. Bauch, and Z. Abu-Shaban, "Harnessing NLOS components for position and orientation estimation in 5G millimeter wave MIMO," *IEEE Trans. Wireless Commun.*, vol. 18, no. 1, pp. 93–107, Jan. 2019.

[18] Z. Abu-Shaban, X. Zhou, T. Abhayapala, G. Seco-Granados, and H. Wymeersch, "Error bounds for uplink and downlink 3D localization in 5G millimeter wave systems," *IEEE Trans. Wireless Commun.*, vol. 17, no. 8, pp. 4939–4954, Aug. 2018.

[19] Z. Lin, T. Lv, and P. T. Mathiopoulos, "3-D indoor positioning for millimeter-wave massive MIMO systems," *IEEE Trans. Commun.*, vol. 66, no. 6, pp. 2472–2486, Jun. 2018.

[20] H. Deng and A. Sayeed, "Mm-wave MIMO channel modeling and user localization using sparse beamspace signatures," in *Proc. IEEE 15th Int. Workshop Signal Process. Adv. Wireless Commun. (SPAWC)*, Jun. 2014, pp. 130–134.

[21] J. Talvitie, M. Valkama, G. Destino, and H. Wymeersch, "Novel algorithms for high-accuracy joint position and orientation estimation in 5G mmWave systems," in *Proc. IEEE Globecom Workshops (GC Wkshps)*, Dec. 2017, pp. 1–7.

[22] R. Mendrzik, H. Wymeersch, and G. Bauch, "Joint localization and mapping through millimeter wave MIMO in 5G systems," in *Proc. IEEE Global Commun. Conf. (GLOBECOM)*, Dec. 2018, pp. 1–6.

[23] Z. Lin, T. Lv, J. A. Zhang, and R. P. Liu, "3D wideband mmWave localization for 5G massive MIMO systems," in *Proc. IEEE Global Commun. Conf. (GLOBECOM)*, Dec. 2019, pp. 1–6.

[24] F. Zhu, A. Liu, and V. K. N. Lau, "Channel estimation and localization for mmWave systems: A sparse Bayesian learning approach," in *Proc. IEEE Int. Conf. Commun. (ICC)*, May 2019, pp. 1–6.

[25] R. Mendrzik, F. Meyer, G. Bauch, and M. Win, "Localization, mapping, and synchronization in 5G millimeter wave massive MIMO systems," in *Proc. IEEE 20th Int. Workshop Signal Process. Adv. Wireless Commun. (SPAWC)*, Jul. 2019, pp. 1–5.

[26] M. Ruble and I. Güvenç, "Wireless localization for mmWave networks in urban environments," *EURASIP J. Adv. Signal Process.*, vol. 2018, no. 1, pp. 1–19, Dec. 2018.

[27] O. Kanhere, S. Ju, Y. Xing, and T. S. Rappaport, "Map-assisted millimeter wave localization for accurate position location," in *Proc. IEEE Global Commun. Conf. (GLOBECOM)*, Dec. 2019, pp. 1–6.

[28] F. Lemic, J. Martin, C. Yarp, D. Chan, V. Handziski, R. Brodersen, G. Fettweis, A. Wolisz, and J. Wawrzynek, "Localization as a feature of mmWave communication," in *Proc. Int. Wireless Commun. Mobile Comput. Conf. (IWCMC)*, Sep. 2016, pp. 1033–1038.

[29] H. El-Sayed, G. Athanasiou, and C. Fischione, "Evaluation of localization methods in millimeter-wave wireless systems," in *Proc. IEEE 19th Int. Workshop Comput. Aided Model. Design Commun. Links Netw. (CAMAD)*, Dec. 2014, pp. 345–349.

[30] N. Garcia, H. Wymeersch, E. G. Larsson, A. M. Haimovich, and M. Coulon, "Direct localization for massive MIMO," *IEEE Trans. Signal Process.*, vol. 65, no. 10, pp. 2475–2487, May 2017.

[31] D. Dardari and F. Guidi, "Direct position estimation from wavefront curvature with single antenna array," in *Proc. 8th Int. Conf. Localization GNSS (ICL-GNSS)*, Jun. 2018, pp. 1–5.

[32] H. Wymeersch, N. Garcia, H. Kim, G. Seco-Granados, S. Kim, F. Wen, and M. Fröhle, "5G mm wave downlink vehicular positioning," in *Proc. IEEE Global Commun. Conf. (GLOBECOM)*, Dec. 2018, pp. 206–212.

[33] H. Kim, H. Wymeersch, N. Garcia, G. Seco-Granados, and S. Kim, "5G mmWave vehicular tracking," in *Proc. 52nd Asilomar Conf. Signals, Syst., Comput.*, Oct. 2018, pp. 541–547.

[34] J. Palacios, P. Casari, and J. Widmer, "JADE: Zero-knowledge device localization and environment mapping for millimeter wave systems," in *Proc. IEEE Conf. Comput. Commun. (INFOCOM)*, May 2017, pp. 1–9.

[35] M. Aladsani, A. Alkhateeb, and G. C. Trichopoulos, "Leveraging mmWave imaging and communications for simultaneous localization and mapping," in *Proc. IEEE Int. Conf. Acoust., Speech Signal Process. (ICASSP)*, May 2019, pp. 4539–4543.

[36] A. Yassin, Y. Nasser, A. Y. Al-Dubai, and M. Awad, "MOSAIC: Simultaneous localization and environment mapping using mmWave without a-priori knowledge," *IEEE Access*, vol. 6, pp. 68932–68947, 2018.

[37] J. He, H. Wymeersch, L. Kong, O. Silven, and M. Juntti, "Large intelligent surface for positioning in millimeter wave MIMO systems," in *Proc. IEEE 91st Veh. Technol. Conf. (VTC-Spring)*, May 2020, pp. 1–5.

[38] J. He, H. Wymeersch, T. Sanguanpuak, O. Silven, and M. Juntti, "Adaptive beamforming design for mmWave RIS-aided joint localization and communication," in *Proc. IEEE Wireless Commun. Netw. Conf. Workshops (WCNCW)*, Apr. 2020, pp. 1–6.

[39] B. P. Zhou, A. Liu, and V. Lau, "Successive localization and beamforming in 5G mmWave MIMO communication systems," *IEEE Trans. Signal Process.*, vol. 67, no. 6, pp. 1620–1635, Mar. 2019.

[40] M. Z. Comiter, M. B. Crouse, and H. T. Kung, "A data-driven approach to localization for high frequency wireless mobile networks," in *Proc. IEEE Global Commun. Conf. (GLOBECOM)*, Dec. 2017, pp. 1–7.

[41] T. Koike-Akino, "Fingerprinting-based indoor localization with commercial mmWave WiFi: A deep learning approach," *IEEE Access* vol. 8, pp. 84879–84892, 2020.

[42] U. Bhattacherjee, C. K. Anjinappa, L. Smith, E. Ozturk, and I. Guvenc, "Localization with deep neural networks using mmWave ray tracing simulations," in *Proc. SoutheastCon*, Mar. 2020, pp. 1–8.

[43] J. Walfisch and H. L. Bertoni, "A theoretical model of UHF propagation in urban environments," *IEEE Trans. Antennas Propag.*, vol. AP-36, no. 12, pp. 1788–1796, Dec. 1988.

[44] N. Kita, W. Yamada, and A. Sato, "Path loss prediction model for the over-rooftop propagation environment of microwave band in suburban areas," *Electron. Commun. Jpn. (I, Commun.)*, vol. 90, no. 1, pp. 13–24, Jan. 2007.

[45] K. Murakami, P. Hanpinitsak, J. Takada, and K. Saito, "Characterization of dominant propagation mechanism for fixed wireless access link in the sub-urban area at 26 GHz band," in *Proc. 2nd Post-IRACON Meeting*, 2021, pp. 1–3.

[46] P. Hanpinitsak, K. Murakami, J. Takada, and K. Saito, "Characterization of dominant propagation mechanism for fixed wireless access link in the sub-urban area at 26 GHz band," *IEEE Access*, to be published.

[47] S. C. Nardone, A. G. Lindgren, and K. F. Gong, "Fundamental properties and performance of conventional bearings-only target motion analysis," *IEEE Trans. Autom. Control*, vol. AC-29, no. 9, pp. 775–787, Sep. 1984.
[48] K. Dogancay and G. Ibal, "Instrumental variable estimator for 3D bearings-only emitter localization," in *Proc. Int. Conf. Intell. Sensors, Sensor Netw. Inf. Process.*, 2005, pp. 63–68.
[49] A. Molisch, *Wireless Communications*, 2nd ed. Hoboken, NJ, USA: Wiley, 2005.
[50] R. G. Kouyoumjian and P. H. Pathak, "A uniform geometrical theory of diffraction for an edge in a perfectly conducting surface," *Proc. IEEE*, vol. 62, no. 11, pp. 1448–1461, Nov. 1974.
[51] P. Hanpinitsak, K. Saito, and J. Takada, "Emitter localization method and program," Japan Patent 20 200 127, Oct. 30, 2020.
[52] N. Czink, P. Cera, J. Salo, E. Bonek, J.-P. Nuutinen, and J. Ylitalo, "A framework for automatic clustering of parametric MIMO channel data including path powers," in *Proc. IEEE Veh. Technol. Conf.*, Sep. 2006, pp. 1–5.
[53] D. W. Marquardt, "An algorithm for least-squares estimation of nonlinear parameters," *J. Soc. Ind. Appl. Math.*, vol. 11, no. 2, pp. 431–441, 1963.
[54] *Reference Radiation Patterns of Omnidirectional, Sectoral and Other Antennas for the Fixed and Mobile Services for Use in Sharing Studies in the Frequency Range From 400 MHz to about 70 GHz*, document Rec. ITU-R F.1336-5, Jan. 2019.
[55] P. Hanpinitsak, K. Murakami, K. Saito, and J.-I. Takada, "Angle-of-arrival-based outdoor localization for spectrum sharing at 25 GHz band," in *Proc. Int. Symp. Antennas Propag. (ISAP)*, Jan. 2021.
[56] K. Haneda, S. L. H. Nguyen, J. Jarvelainen, and J. Putkonen, "Estimating the omni-directional pathloss from directional channel sounding," in *Proc. 10th Eur. Conf. Antennas Propag. (EuCAP)*, Apr. 2016, pp. 1–5.
[57] J. Vehmas, J. Jarvelainen, S. L. H. Nguyen, R. Naderpour, and K. Haneda, "Millimeter-wave channel characterization at Helsinki airport in the 15, 28, and 60 GHz bands," in *Proc. IEEE 84th Veh. Technol. Conf. (VTC-Fall)*, Sep. 2016, pp. 1–5.
[58] P. Hanpinitsak, K. Saito, J.-I. Takada, M. Kim, and L. Materum, "Multi-path clustering and cluster tracking for geometry-based stochastic channel modeling," *IEEE Trans. Antennas Propag.*, vol. 65, no. 11, pp. 6015–6028, Nov. 2017.
[59] S. Mota, M. O. Garcia, A. Rocha, and F. Pérez-Fontán, "Clustering of the multipath radio channel parameters," in *Proc. 5th Eur. Conf. Antennas Propag. (EUCAP)*, Apr. 2011, pp. 3232–3236.
[60] M. Steinbauer, H. Ozcelik, H. Hofstetter, C. F. Mecklenbrauker, and E. Bonek, "How to quantify multipath separation," *IEICE Trans. Electron.*, vol. 85, no. 3, pp. 552–557, 2002.
[61] *Zenrin: Maps to the Future: 3D Map Data*. Accessed: Apr. 15, 2022. [Online]. Available: https://www.zenrin.co.jp/product/category/gis/contents/3d/index.html

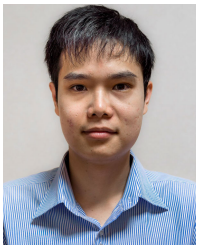

PANAWIT HANPINITSAK (Member, IEEE) was born in 1991. He received the B.E. degree (Hons.) in electronics and communications engineering from the Sirindhorn International Institute of Technology, Thammasat University, Pathumthani, Thailand, in 2013, and the M.E. and D.E. degrees from the Tokyo Institute of Technology, Japan, in 2016 and 2019, respectively.

He was a Guest Ph.D. Researcher at Aalborg University, Denmark, and the Ilmenau University of Technology, Germany, in 2016 and 2018, respectively. He was a Researcher at the Tokyo Institute of Technology, from 2019 to 2021. He is currently a Lecturer at the Department of Computer Engineering, Khon Kaen University, Thailand. His research interests include localization, artificial intelligence, machine learning, computer vision, and the Internet of Things.

KOSUKE MURAKAMI (Student Member, IEEE) was born in 1993. He received the B.E. degree from the National College of Technology, Sendai, in 2016, and the M.E. degree from the Tokyo Institute of Technology, Japan, in 2018, where he is currently pursuing the Ph.D. degree. His research interests include radio propagation channel modeling, measurement, and spectrum sensing in cognitive radio. He received the Best Student Presentation Award at the IEICE Short RangeWireless (SRW) Conference in 2018. He is a member of the IEICE.

JUN-ICHI TAKADA (Senior Member, IEEE) received the B.E., M.E., and D.E. degrees in electrical and electronic engineering from the Tokyo Institute of Technology, Tokyo, Japan, in 1987, 1989, and 1992, respectively.

He was a Research Associate with Chiba University, Chiba, Japan, from 1992 to 1994, and an Associate Professor with the Tokyo Institute of Technology, from 1994 to 2006. He was also a Researcher with the National Institute of Information and Communications Technology, Kanagawa, Japan, from 2003 to 2007. He has been a Professor at the Tokyo Institute of Technology, since 2006. His research interests include radio-wave propagation and channel modeling for mobile and short-range wireless systems, regulatory issues of spectrum sharing, and ICT applications for international development.

Dr. Takada is a fellow of the IEICE, Japan.

KENTARO SAITO (Member, IEEE) was born in Kanagawa, Japan, in 1977. He received the B.S. and Ph.D. degrees from the University of Tokyo, Japan, in 2002 and 2008, respectively.

He joined NTT DOCOMO, Kanagawa, in 2002. Since then, he has been engaged in research and development of mobile communication systems and radio propagation. He joined the Tokyo Institute of Technology, Japan, in 2015. Since then, he has been engaged in research on radio propagation for mobile communication systems.

Dr. Saito is a member of the IEICE.